

Investigating the Event-Shape Methods in Search for the Chiral Magnetic Effect in Relativistic Heavy Ion Collisions

Han-Sheng Li,^{1,*} Yicheng Feng,^{1,†} and Fuqiang Wang^{1,‡}

¹*Department of Physics and Astronomy, Purdue University, West Lafayette, IN 47907*

The Chiral Magnetic Effect (CME) is a phenomenon in which electric charge is separated by a strong magnetic field from local domains of chirality imbalance and parity violation in quantum chromodynamics (QCD). The CME-sensitive observable, charge-dependent three-point azimuthal correlator $\Delta\gamma$, is contaminated by a major physics background proportional to the particle's elliptic anisotropy v_2 . Event-shape engineering (ESE) binning events in dynamical fluctuations of v_2 and event-shape selection (ESS) binning events in statistical fluctuations of v_2 are two methods to search for the CME by projecting $\Delta\gamma$ to the $v_2 = 0$ intercept. We conduct a systematic study of these two methods using physics models as well as toy model simulations. It is observed that the ESE method requires significantly more statistics than the ESS method to achieve the same statistical precision of the intercept. It is found that the intercept from the ESS method depends on the details of the event content, such as the mixtures of background-contributing sources, and thus is not a clean measure of the CME.

I. INTRODUCTION

It has been predicted by quantum chromodynamics (QCD) that vacuum fluctuations can result in gluon fields of non-zero topological charges in local metastable domains. Interactions of quarks with such gluon fields can cause chirality imbalance, breaking the parity and charge-parity symmetries in those domains. Such chirality imbalance, under a strong magnetic field, would result in charge separation, a phenomenon called the chiral magnetic effect (CME) [1–4].

Ultra-strong magnetic fields are presumably produced in non-head-on relativistic heavy ion collisions [5, 6]. The magnetic field is on average perpendicular to the reaction plane (RP, the plane span by the beam and the impact parameter direction of the collision). The CME-induced charge separation is along the direction of the magnetic field, and may be conveniently quantified by the a_1 variable in Fourier series of particle azimuthal distributions [7],

$$dN_{\pm}/d\phi^* \propto 1 \pm 2a_1 \sin \phi^* + 2v_2 \cos 2\phi^* + \dots, \quad (1)$$

where ϕ^* is the azimuthal angle of the particle momentum vector with respect to the RP and the subscript ‘ \pm ’ indicates particle charge sign. The elliptic anisotropy v_2 harmonic is the leading modulation in particle distributions produced in relativistic heavy ion collisions [8]. Because of a vanishing mean a_1 due to random fluctuations, a commonly used observable is the three-point correlator [7],

$$\gamma = \langle \cos(\phi_\alpha + \phi_\beta - 2\psi) \rangle, \quad (2)$$

where ϕ_α and ϕ_β are the azimuthal angles of two particles of interest (POI). To cancel charge-independent

backgrounds, such as effects from global momentum conservation, the difference between opposite-sign (OS) and same-sign (SS) correlators is used [9],

$$\Delta\gamma \equiv \gamma_{os} - \gamma_{ss}. \quad (3)$$

The CME signal presented in the $\Delta\gamma$ observable would then be $2a_1^2$.

Definite signals of the CME have not yet been observed [9–13]. The major difficulty is the large contamination in $\Delta\gamma$ from mundane QCD backgrounds. Those backgrounds arise from genuine two-particle correlations, such as correlations between daughter particles from a resonance decay, or among particles from the same jet or back-to-back dijet, coupled with elliptic anisotropies of those background sources [7, 14–16]. This background correlation can be schematically expressed as [7, 17]

$$\Delta\gamma_{res} = \langle \cos(\phi_\alpha + \phi_\beta - 2\phi_{res}) \rangle v_{2,res}, \quad (4)$$

where the subscript ‘res’ stands generically for correlated two-particle clusters such as resonances and jets, and $v_{2,res} \equiv \langle \cos 2(\phi_{res} - \psi) \rangle$ is the elliptic flow anisotropy of those background-contributing sources.

Large efforts have since been invested to eliminate or mitigate those backgrounds [18–22], including innovative observables [23–28]. One of the techniques is the event-shape engineering (ESE) [23, 24, 29] method, grouping events into classes of different v_2 values relying on the dynamical fluctuations of v_2 . A variation of this method is to select events according to the particle emission pattern, called the event-shape selection (ESS) method [30], relying on the statistical fluctuations of v_2 . The main difference between the two methods is in the ways of quantifying the event shape. The ESE method [29] uses a variable calculated *not* from the particles of interest (POI) that are used for the physics measurement of $\Delta\gamma$, while the ESS method uses a variable calculated from the POIs [30]. Each method analyzes $\Delta\gamma$ as a function of v_2 in events binned according to the corresponding event-shape variable and projects $\Delta\gamma$ to $v_2 = 0$ to obtain the

* li3924@purdue.edu

† feng216@purdue.edu

‡ fqwang@purdue.edu

intercept, presumably insensitive to backgrounds. While the ESE method is relatively straightforward to comprehend, the ESS method is complex because the POIs are used in both event selection and physics measurement. In this paper, we conduct a systematic study of the ESS and ESE methods for the CME search using several physics models as well as toy models of varying ingredients, with the goal to elucidate what the projected intercept entails from each method.

The rest of the paper is organized as follows. Section II describes the details of the ESE and ESS methods (and a related early method [18]) used for the CME search. Section III gives brief descriptions of the models used in this study. Section IV presents our model simulation results using ESS and ESE and discusses the findings. Finally, a summary is given in Section V. The appendix compiles all the $\Delta\gamma$ vs. v_2 plots from the simulations by the ESS and ESE methods.

II. THE EVENT-SHAPE TECHNIQUES

In ESE [29], events from a narrow centrality bin are grouped according to the elliptic flow vector magnitude q_2 calculated from particles (or other detected signals in experiment like energy depositions in calorimeters) that are different from the POIs. The event-by-event q_2 quantity is generally defined as

$$\begin{aligned} q_2^2 &= \frac{1}{N} \left[\left(\sum_{i=1}^N \cos 2\phi_i \right)^2 + \left(\sum_{i=1}^N \sin 2\phi_i \right)^2 \right] \\ &= 1 + \frac{1}{N} \sum_{i \neq j} \cos 2(\phi_i - \phi_j), \end{aligned} \quad (5)$$

where N is the number of particles in the event within a given phase space (we use ‘‘particles’’ in our description for convenience without loss of generality). One may use the normalized \hat{q}_2 quantity [30] for ESE,

$$\hat{q}_2^2 \equiv q_2^2 / \langle q_2^2 \rangle. \quad (6)$$

The average of q_2^2 over all events, assuming Poisson fluctuations in multiplicity, is given by

$$\langle q_2^2 \rangle \approx 1 + N v_{2,q}^2 \{2\}, \quad (7)$$

where

$$v_2^2 \{2\} = \langle \cos 2(\phi_1 - \phi_2) \rangle, \quad (8)$$

is the two-particle cumulant elliptic flow anisotropy (ϕ_1 and ϕ_2 are the azimuthal angles of the pair), and the subscript ‘ q ’ in $v_{2,q}$ indicates that it is calculated from the particles used for computing q_2^2 .

In ESE, the q_2^2 is typically measured at forward and backward rapidities [23, 24]. The event classes selected by q_2 (or equivalently q_2^2 or \hat{q}_2^2) within a given narrow centrality range will have different average $\langle v_2 \rangle$ in the

midrapidity region, or any other phase space regions displaced from that for q_2^2 computation. In other words, because q_2 is correlated with $\langle v_2 \rangle$, ESE is dividing events in groups of varying $\langle v_2 \rangle$, which *dynamically* fluctuates from event to event. These dynamical fluctuations are mainly caused by initial geometry fluctuations within the given narrow centrality bin [31, 32].

Since the ESE method selects events according to dynamical fluctuations of the $\langle v_2 \rangle$ of the POIs, decoupled from the q_2^2 computation, it is guaranteed that the average resonance $\langle v_{2,\text{res}} \rangle$, or generally the elliptic anisotropies of all elements in the event including all CME background sources, are proportional to $\langle v_2 \rangle$. Note that the final-state $\langle v_2 \rangle$ contains contributions not only from primordial particles, but also from all decay products of resonances and clusters. Since the averages $\langle v_{2,\text{res}} \rangle$ and $\langle v_2 \rangle$ in those q_2 -selected event classes are all connected to the initial geometry, they are all proportional to each other. This is illustrated in the cartoon in Fig. 1 (left), where the three ellipses illustrate event selections by q_2 and the hollow circles are the average $\langle v_2 \rangle$ and $\langle v_{2,\text{res}} \rangle$ in each q_2 -selected event class. In the ESE analyses for CME searches [23, 24], one analyzes $\Delta\gamma$ as a function of $\langle v_2 \rangle$ in each event class and projects the $\Delta\gamma$ measurement to zero $\langle v_2 \rangle$. The ESE method guarantees that the elliptic flows of the background sources also vanish at zero $\langle v_2 \rangle$. In other words, a linear projection to $\langle v_2 \rangle = 0$ would be equivalent to a projection to $\langle v_{2,\text{res}} \rangle = 0$, where the CME backgrounds are zero. Since all those events are from a narrow centrality bin where the CME signal does not vary much, the intercept of the linear projection is presumably the CME signal. Note that there may still be complications from nonflow contamination [33] depending on how $\Delta\gamma$ and $\langle v_2 \rangle$ are measured, which is outside the scope of the present work.

Since the CME background comes from the elliptic anisotropies imprinted in the particles of interests (POI), it is interesting to select events with an event-shape ellipticity $v_2^{\text{obs}} \equiv \langle \cos 2(\phi - \psi) \rangle$ calculated by POIs themselves (where the EP ψ is determined in another phase space away from the POIs) and examine the $\Delta\gamma$ observable as a function of v_2^{obs} . This method selects on the event-by-event elliptic-shape quantity (particle emission pattern) v_2^{obs} which can fluctuate even to negative values because of large statistical fluctuations, the intercept at $v_2^{\text{obs}} = 0$, more sensitive to the CME, can be well determined from data. This event-shape (ES) analysis was carried out by STAR [18] and the intercept of the linear fit is consistent with zero with the then-available statistics. However, the backgrounds are not determined by v_2^{obs} but by $\langle v_{2,\text{res}} \rangle$. Statistically fluctuated $v_2^{\text{obs}} = 0$ does not necessarily guarantee $\langle v_{2,\text{res}} \rangle = 0$. This is illustrated by the cartoon in Fig. 1 (center). Although $\langle v_{2,\text{res}} \rangle$ is proportional to $\langle v_2 \rangle$ with an unbiased event selection, the strongly (maximally) biased selection of events by v_2^{obs} will obscure the relationship of the averages $\langle v_{2,\text{res}} \rangle$ and v_2^{obs} in each bin of v_2^{obs} of those events, as indicated by the hollow box in Fig. 1 (center). Because of the

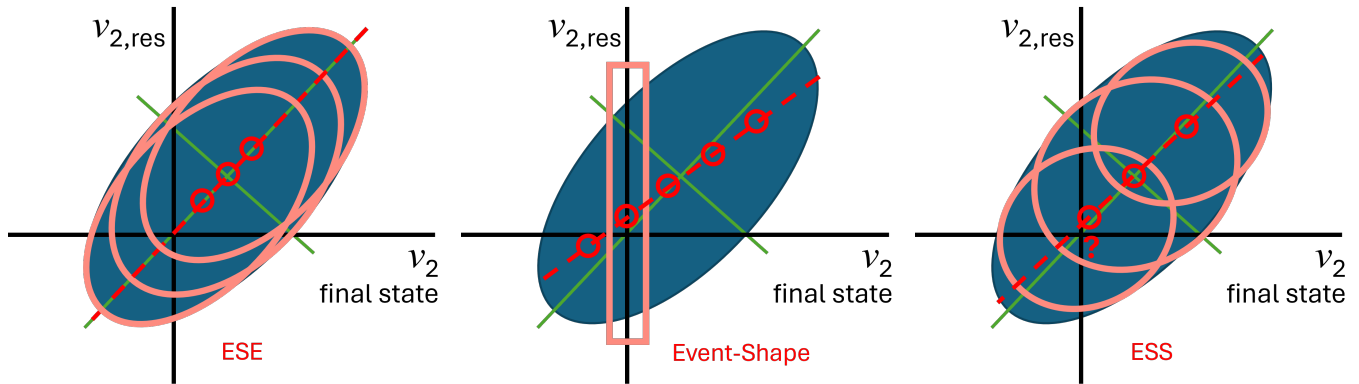


FIG. 1. Cartoons illustrating the various event-shape methods in terms of the event-by-event resonance $v_{2,\text{res}}$ vs. final-state single particle v_2 in events within a narrow centrality bin. Here $v_{2,\text{res}}$ and v_2 are taken to be the event-by-event elliptic shape variables, $\langle \cos 2(\phi - \psi) \rangle$, with respect to the event plane ψ from another phase space different from the particles of interest (POI). (Left panel) Event-Shape Engineering (ESE) where events are selected according to q_2 in phase space region displaced from that of POIs', in which the average $\langle v_{2,\rho} \rangle$ is proportional to $\langle v_2 \rangle$, unbiased, and the spread in $\langle v_2 \rangle$ and $\langle v_{2,\text{res}} \rangle$ are due to dynamical fluctuations. (Center panel) Event-Shape (ES) method where events are binned in the observed elliptic shape variable v_2^{obs} of POIs, and the average $v_{2,\text{res}}$ in those events are strongly biased, not strictly proportional to v_2^{obs} and with a positive $v_{2,\text{res}}$ value at $v_2^{\text{obs}} = 0$. The wide range in v_2^{obs} (including negative values) is mainly due to statistical fluctuations. (Right panel) Event-Shape Selection (ESS) where events are selected according to $\hat{q}_{2,\text{pair}}^2$ of pairs of POIs in which the $v_{2,\text{res}}$ is unnecessarily proportional to v_2 due to complicated biases from the $\hat{q}_{2,\text{pair}}^2$ selection using the same POIs as for v_2 . The wide spreads in v_2 and $v_{2,\text{res}}$ are mainly due to statistical fluctuations inherited in the ESS method involving the same POIs.

overall positive means $\langle v_2^{\text{obs}} \rangle = \langle v_2 \rangle$ and $\langle v_{2,\text{res}} \rangle$ over the entire event sample, the linear projection will give a positive intercept of $\langle v_{2,\text{res}} \rangle$ at $v_2^{\text{obs}} = 0$. In other words, with finite positive average $\langle v_2 \rangle$ in heavy ion collisions, $\langle v_{2,\text{res}} \rangle > 0$ at $v_2^{\text{obs}} = 0$ with events binned in v_2^{obs} . This has been verified by model study [34]. Thus, positive residual background remains in the linear fit intercept in the analysis of $\Delta\gamma$ as a function of v_2^{obs} [18], although the background is significantly reduced compared to that in the inclusive $\Delta\gamma$ measurement. Ideally, in the ES analysis, one would want to select events with the v_2^{obs} values of all resonances (background sources) to be zero, however, such selection is experimentally insurmountable.

It has been recently proposed by Xu *et al.* [30] to select events according to the $\hat{q}_{2,\text{POI}}^2$ of the POIs, and study the $\Delta\gamma$ as a function of v_2 of the POIs. This is similar in spirit to the ES method above where the events are selected by v_2^{obs} and the $\Delta\gamma$ is examined as a function of the same v_2^{obs} variable. Here, the selection variable $\hat{q}_{2,\text{POI}}^2$ and the v_2 variable are different, although related as they are computed by the same POIs. The \hat{q}_2^2 variable is an event-by-event quantity connected to two-particle cumulant anisotropy (cf Eq. 5), whereas v_2 can be measured with respect to ψ from another phase space like in the ES method. (Of course v_2 can also be computed by the two-particle cumulant method, in which case it is more directly connected to \hat{q}_2^2 .) The variations in the event-by-event $\hat{q}_{2,\text{POI}}^2$ quantity, within a given narrow centrality bin, are mainly from statistical fluctuations. Since the v_2 in those $\hat{q}_{2,\text{POI}}^2$ -selected events are related to $\hat{q}_{2,\text{POI}}^2$ itself, the variations in v_2 is also primarily of statistical nature. (Note, we simply use v_2 here, instead of the $\langle v_2 \rangle$ for ESE,

to indicate that the v_2 in ESS is of statistical nature although it is an ‘‘average’’ v_2 in events selected by $\hat{q}_{2,\text{POI}}^2$.) Since this technique selects on the statistical fluctuations in event shape, not on the dynamical fluctuations in $\langle v_2 \rangle$ like in the ESE method, it is called the Event-Shape-Selection (ESS) method [30]. The most important difference in the ESS method from the ESE method is that the \hat{q}_2^2 is computed from the POIs in the former but in the later the phase-space where to compute \hat{q}_2^2 is displaced from that of the POIs'. In both approaches, one groups events (within a given narrow centrality bin) according to \hat{q}_2^2 and studies the $\Delta\gamma$ variable as a function of the v_2 of the POIs.

Several combinations of $\hat{q}_{2,\text{POI}}^2$ and v_2 variables have been investigated in Ref. [30]. The $q_{2,\text{POI}}^2$ can be computed using single particle azimuthal angles of the POIs by Eq. 5. It can also be defined by pairs of POIs similar to Eq. 5; in this case, the $q_{2,\text{pair}}^2$ of pairs is calculated by substituting the i^{th} particle's ϕ_i by the azimuthal angle of the i^{th} pair in Eq. 5, and the sum runs over all pairs of POIs in the event. The normalized $\hat{q}_{2,\text{pair}}^2$ is then

$$\hat{q}_{2,\text{pair}}^2 \equiv q_{2,\text{pair}}^2 / \langle q_{2,\text{pair}}^2 \rangle. \quad (9)$$

where $\langle q_{2,\text{pair}}^2 \rangle \approx 1 + N_{\text{pair}} v_{2,\text{pair}}^2 \{2\}$. Similarly, one can define v_2 to be that of single particles of POIs or that of pairs of POIs; in the latter, one replace the azimuthal angle ϕ of a single particle by that of a particle pair in

$$v_2 = \langle \cos 2(\phi - \psi) \rangle. \quad (10)$$

One can study the $\Delta\gamma$ as a function of v_2 of single POI particles (or $v_{2,\text{pair}}$ of pairs of POI particles) selecting

events on $\hat{q}_{2,\text{POI}}^2$ of single POIs (or $\hat{q}_{2,\text{pair}}^2$ of pairs of POIs). It is found by the Anomalous-Viscous Fluid Dynamics (AVFD) model study that, out of the four combinations, it is the best to use the combination of pair $\hat{q}_{2,\text{pair}}^2$ and single $v_{2,\text{single}}$ [30], because the linear intercept of $\Delta\gamma$ as a function of $v_{2,\text{single}}$ of single POIs selecting events on $\hat{q}_{2,\text{pair}}^2$ of pairs of POIs reflects most closely the true CME in AVFD. However, since the same POIs are used for $\hat{q}_{2,\text{pair}}^2$, $v_{2,\text{single}}$ and $\Delta\gamma$, self-correlations are present in the measurement whose effects/biases are hard to discern. It is unclear how much background is remaining in the ESS intercept, and whether the remaining background is positive or negative. This is illustrated by the cartoon in Fig. 1 (right). In this work, we focus on the best combination of pair $\hat{q}_{2,\text{pair}}^2$ and single $v_{2,\text{single}}$ in ESS as found in [30], and examine what possible biases there may exist and the possible level of remaining background in the ESS intercept.

III. MODEL SETUP AND ANALYSIS DETAILS

We have investigated four physics models that have been used to simulate heavy ion collisions. Three of them are dynamical models (AVFD, AMPT, EPOS) and one is a parameterization model (HYDJET++). The AVFD model is a model designed to study CME-related physics and has the capability to implement axial charge current and magnetic field. The other three models do not have those CME capabilities and are useful only for background studies which are the main purpose of this work. The centralities of the models are determined by the charged hadron multiplicity within $|\eta| < 0.5$ as in experiments [35].

For further insights, we have also investigate background behaviors with two versions of a toy model. The inputs to the toy models are parameterizations of measured data.

A. AVFD Model

The AVFD model [36–38] is an anomalous fluid dynamics developed to describe the evolution of chiral fermion currents in the quark-gluon plasma (QGP) created in relativistic heavy ion collisions in addition to the normal VISHNU simulations [39]. The average magnetic field is calculated from the spectator protons and it is nominally along the direction perpendicular to the RP. In the model, the magnetic field is quantified by event-by-event simulations [40] taking into account the fluctuations of the magnetic field direction with respect to the RP. A modest time evolution is assumed for the decreasing magnetic field with a typical lifetime comparable to the initial time of hydrodynamic evolution ~ 0.6 fm/ c . The initial condition for the axial charge density (n_5) is dynamically generated in AVFD to be proportional to the entropy density (s), and the strength is set via the

proportionality coefficient n_5/s . Three n_5/s values are used in the simulations, $n_5/s=0, 0.1, \text{ and } 0.2$. The QGP medium evolution is simulated by viscous hydrodynamics to describe the bulk background in heavy ion collisions, with transport parameters for the diffusion coefficient as well as the relaxation time. A final hadronic stage after the hydrodynamic freeze-out is included with hadronic re-scatterings and resonance decays.

Au+Au collisions are simulated by AVFD at $\sqrt{s_{NN}} = 200$ GeV. In this study we focus on the centrality range of 30–40% [28]. Figure 2 (upper left) shows the difference of the m_{inv} distributions between OS and SS pairs for the three values of n_5/s . The CME implemented in AVFD affects the relative OS and SS pair m_{inv} distributions—the distribution flattens with larger n_5/s . This arises from contributions from back-to-back OS pairs (hence larger m_{inv}) and near-side SS pairs (hence smaller m_{inv}) as a result of the CME, resulting in an enhancement at large m_{inv} and depletion at small m_{inv} for large n_5/s compared to small one. Several resonance peaks are apparent in the m_{inv} distributions, ρ^0 , $f_0(980)$, and $f_2(1270)$. No intrinsic mass width is implemented in AVFD, so the resonances appear as δ -functions. Weak-decay hadrons are treated as stable particles in AVFD, so no K_S peak is present in the m_{inv} distribution.

B. AMPT Model

AMPT (A Multi-Phase Transport) is a parton transport model [41]. It consists of a fluctuating initial condition, parton elastic scatterings, quark coalescence for hadronization, and hadronic interactions. The initial condition of AMPT is based on the HIJING model [42]. The string melting version of AMPT, which we use for our study, converts these initial hadrons into their valence quarks and antiquarks [41, 43]. The (anti-)quarks further evolve via two-body elastic scatterings, treated with Zhang’s parton cascade [44] with a total parton scattering cross section of 3 mb. After parton scatterings cease, a simple quark coalescence model is applied to convert partons into hadrons [41]. Subsequent interactions of those formed hadrons are modeled by a hadron cascade, including meson-meson, meson-baryon, and baryon-baryon elastic and inelastic scatterings [41]. The model has been extensively tested to reproduce the p_T spectra and flows of bulk particles.

Minimum bias (MB) Au+Au collisions are simulated by AMPT at $\sqrt{s_{NN}} = 200$ and 27 GeV. We terminate the hadronic interactions at a cutoff time of 30 fm/ c (by model default). Figure 2 (upper center) shows the difference of the m_{inv} distributions between OS and SS pairs for 30–40% centrality, as an example. The ρ^0 peak is evident. No intrinsic mass width is implemented in AMPT, so the resonance peak is a sharp δ -function. Weak-decay hadrons are treated as stable particles in AMPT, so no K_S peak is present in the m_{inv} distribution.

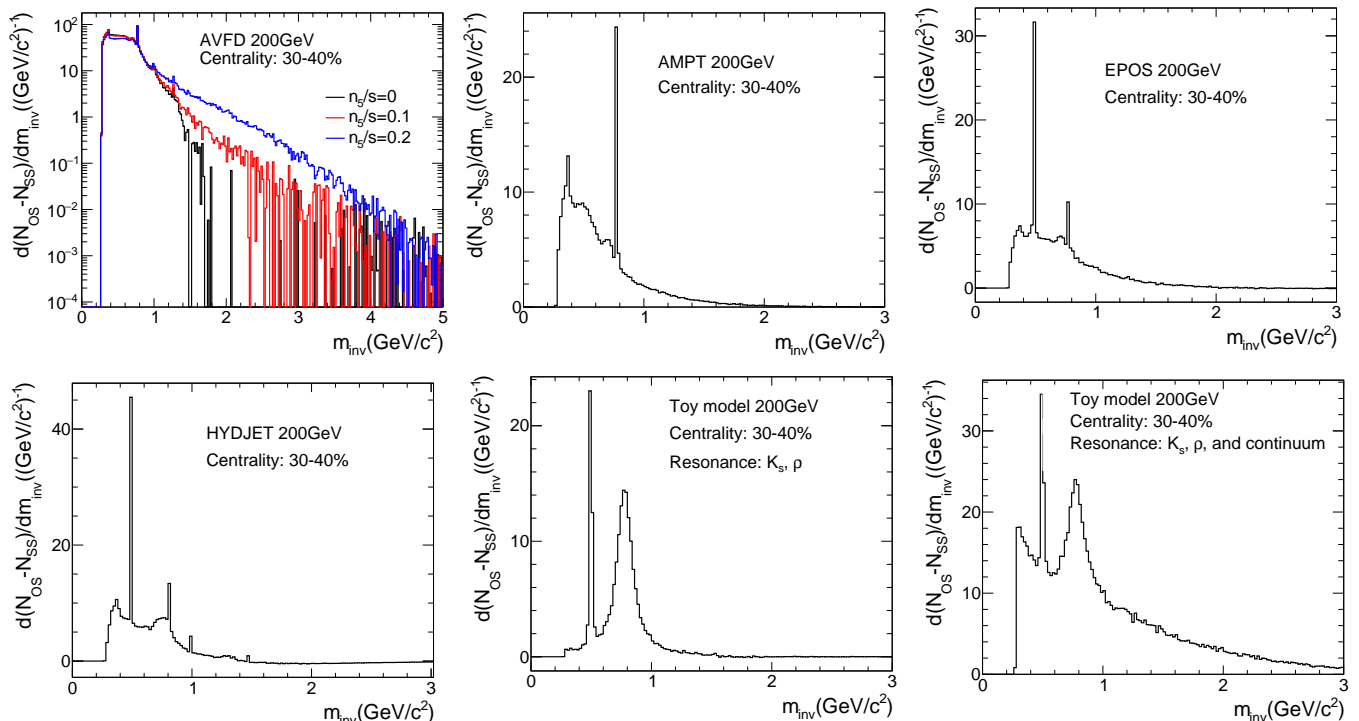


FIG. 2. The m_{inv} distributions. Shown are the OS pair m_{inv} distribution subtracted by the SS pair one from AVFD with axial current densities $n_s/s = 0, 0.1$, and 0.2 (upper left), AMPT (upper center), EPOS4 (upper right), HYDJET++ (lower left), Toy Model I simulation including primordial pions, and K_S and ρ^0 resonance-decay pions (lower center), and Toy Model II simulation including in addition decay pions from a mass continuum (lower right). Particles used to form the m_{inv} distributions are taken from all charged hadrons (defined to be π^\pm , K^\pm , p , and \bar{p} in our study and treated as pions with pion mass) and are from the kinematic range of $|\eta| < 1$ and $0.2 < p_T < 2$ GeV/ c . In the toy models all final-state particles are charged pions.

C. EPOS4 Model

EPOS4 [45] is a Monte Carlo model to simulate high-energy proton-proton and nucleus-nucleus collisions, among others. At high energies many interactions (nucleonic or partonic) happen simultaneously at once, not sequentially. The parallel multi-parton interactions are modeled via the Pomeron exchange mechanism and result in complex configurations composed of many strings [46, 47]. The string decay products further interact, forming a medium treated by the core-corona picture followed by fluid dynamic evolution of the former and ordinary hadronic interactions in the latter [48]. The EPOS4 model has been extensively tested and tuned by proton-proton and heavy ion data.

MB Au+Au collisions are simulated by EPOS4 (version 4.0.0) at $\sqrt{s_{NN}} = 200$ and 27 GeV. Figure 2 (upper right) shows the difference of the m_{inv} distributions between OS and SS pairs for 30–40% centrality, as an example. The K_S and ρ^0 resonance peaks are evident. No intrinsic mass width is implemented in EPOS, so the resonance peaks are sharp δ -functions. All K_S particles are decayed in EPOS and their decay pions are treated as “primordial” POIs.

D. HYDJET++ Model

HYDJET++ is an event generator to simulate heavy ion collisions by combining two independent components, namely, the soft physics part and the hard physics part [49, 50]. The former is determined by thermal equilibrium where hadrons are produced on the hypersurface represented by a parameterization of relativistic hydrodynamics with given freeze-out conditions. Chemical and kinetic freeze-outs are separate, and hadronic resonances are decayed. The hard physics part starts with an initial parton configuration from PYTHIA [51], lets partons rescatter traversing the hot and dense nuclear medium, and losing energy via collisions and radiative gluon emission, and follows with parton hadronization and particle formation. The model parameters are tuned to reproduce heavy ion data on charged particle multiplicity, p_T -spectra and flow.

MB Au+Au collisions are generated by HYDJET++ (version 2.4) at $\sqrt{s_{NN}} = 200$ and 27 GeV. Figure 2 (lower left) shows the difference of the m_{inv} distributions between OS and SS pairs for 30–40% centrality, as an example. The K_S , ρ^0 , and $f_0(980)$ resonance peaks are evident. No intrinsic mass width is implemented in HYDJET, so the resonance peaks are sharp δ -functions. All

K_S particles are decayed in HYDJET and their decay pions are treated as “primordial” POIs.

E. Toy Model I

To gain insights, we have also generated particles using a toy model [34]. Toy models are useful and convenient to investigate the outcome of an analysis method given the known input to the model.

Two versions of the toy model are examined. In Toy Model I, we include primordial pions and two resonances, K_S and ρ^0 . The resonance mass is generated according to the Breit-Wigner distribution of proper mass and width [52]. The primordial pion, K_S , and ρ^0 input information are taken from experimental measurements of Au+Au collisions at 200 GeV in the centrality range of 30–40%, which we currently focus on. We generate particles uniformly within rapidity range of $-1.5 < y < 1.5$, taking event-by-event particle multiplicities according to Poisson statistics about the means of three times the measured average densities [35, 53, 54]. The p_T spectra are parameterized based on the measured data [55, 56], namely,

$$\frac{dN}{dp_T} = \begin{cases} p_T \left[\exp\left(\frac{m_T}{T_{BE}}\right) - 1 \right]^{-1} & \text{for pions, and} \\ p_T \exp\left(-\frac{m_T - m_0}{T}\right) & \text{for resonances,} \end{cases} \quad (11)$$

where transverse momentum $m_T \equiv \sqrt{p_T^2 + m_0^2}$ with m_0 being the rest mass of the corresponding particle. The particle or resonance p_T is sampled from Eq. 11. At a given p_T , the average $\langle v_2 \rangle$ of pion, K_S , or ρ^0 meson is calculate based the following parameterization of data motivated by the number-of-constituent-quark scaling [57],

$$\langle v_2 \rangle(p_T) = \frac{2a}{1 + \exp\left(-\frac{(m_T - m_0)/2 - b}{c}\right)} - 2d. \quad (12)$$

A 40% v_2 fluctuations are included about the parameterized $\langle v_2 \rangle(p_T)$ event-by-event to obtain the final v_2 of the particle, based on which the azimuthal angle is generated about the fixed event plane at $\psi = 0$. All parameters used in the toy model can be found in Ref. [34].

Toy model data are generated, using parameters corresponding to the 30–40% centrality of Au+Au collisions at 200 GeV. Figure 2 (lower center) shows the difference of the m_{inv} distributions between OS and SS pairs. We require all resonances in our toy model (i.e. K_S and ρ^0) to decay into a pair of charged pions. The decay is isotropic in the parent rest frame, and the decay pions are properly boosted to the lab frame. The K_S and ρ^0 resonance peaks are evident.

As default only 2% of the measured K_S abundance are generated in our toy model because this is the approximate fraction of K_S whose decay daughters are both reconstructed as primordial pions in the STAR experiment. We vary this fraction to investigate its effect on our results.

F. Toy Model II

As shown in Fig. 2, all physics models have a mass continuum in the m_{inv} distribution on which the resonance peaks reside. To mimic this, we add a mass continuum in our second version of the toy model. The mass distribution of the continuum is generated according to a probability $\propto e^{-m_{inv}c^2/\text{GeV}}$ between the two-pion mass threshold ($0.28 \text{ GeV}/c^2$) and $5 \text{ GeV}/c^2$. Given a generated mass value, a Breit-Wigner distribution (mean at the mass value and width equal to the ρ^0 width [52]) is sampled to obtain the mass of the continuum “resonance”. All particles in the generated mass continuum are decayed into $\pi^+\pi^-$ isotropically in the parent rest frame. The decay pions are boosted properly to the lab frame.

G. Analysis Details

POIs are taken to be all charged hadrons, defined to be π^\pm , K^\pm , p and \bar{p} in our study, and are within the transverse momentum range of $0.2 < p_T < 2 \text{ GeV}/c$ and a certain central pseudorapidity (η) range, typical of midrapidity detectors such as the STAR experiment [58].

In the ESS method, the POIs are taken to be within $|\eta| < 1$ (or $|\eta| < 2$). The event selection quantity pair $\hat{q}_{2,\text{pair}}^2$ is computed by the two-particle cumulant method in Eqs. 5,9, always using all particle pairs of the same POIs.

In the ESE method, the acceptance $|\eta| < 1$ (or $|\eta| < 2$) is divided into three subevents:

- west subevent: $-1 < \eta < -0.3$ (or $-2 < \eta < -0.3$),
- center subevent: $|\eta| < 0.3$,
- east subevent: $0.3 < \eta < 1$ (or $0.3 < \eta < 2$).

The POIs are taken from either the west subevent or the east subevent, but not from both. The event selection quantity \hat{q}_2^2 is computed by the two-particle cumulant method in Eqs. 5,6, using particles from the center subevent, $|\eta| < 0.3$ (or from a forward/backward region $3 < |\eta| < 4$).

Figure 3 shows the event-by-event $\hat{q}_{2,\text{pair}}^2$ and \hat{q}_2^2 distributions from the ESS and ESE methods, respectively. The two distributions are similar for each of the models; the \hat{q}_2^2 distribution ($|\eta| < 0.3$) is broader than the $\hat{q}_{2,\text{pair}}^2$ distribution ($|\eta| < 1$) because of larger fluctuations in the smaller acceptance. We have checked that the distribution of the single particle \hat{q}_2^2 calculated from $|\eta| < 1$ is similar to the pair $\hat{q}_{2,\text{pair}}^2$ from the same acceptance.

The \hat{q}_2^2 variable calculated from single particles has been widely used. The $\hat{q}_{2,\text{pair}}^2$ variable calculated from particle pairs is relatively new. To gain insights, we calculate by Eq. 8 the two-particle cumulant $v_2\{2\}$ of single particles of the POIs in events grouped by $\hat{q}_{2,\text{pair}}^2$. Such a quantity can also be calculated for particle pairs of POIs,

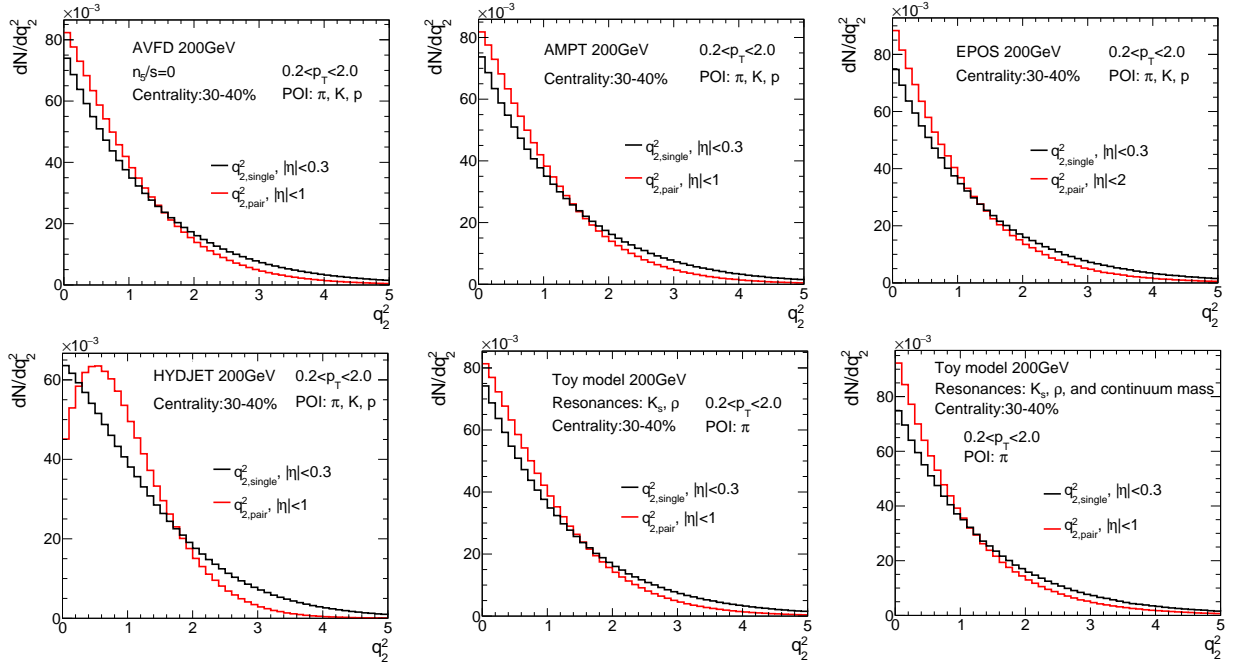


FIG. 3. The q_2^2 distributions. Shown are the single q_2^2 and pair $q_{2,\text{pair}}^2$ distributions of POIs from AVFD with $n_5/s = 0$ (upper left), AMPT (upper center), EPOS (upper right), HYDJET (lower left), Toy Model I (lower center), and Toy Model II (lower right). Shown in all panels are for the 30–40% centrality of Au+Au collisions, as examples. The q_2^2 (used in the ESE analysis) is calculated from particles in $|\eta| < 0.3$, and the pair $q_{2,\text{pair}}^2$ (used in the ESS analysis) is calculated from particles within $|\eta| < 1$, both with $0.2 < p_T < 2$ GeV/c.

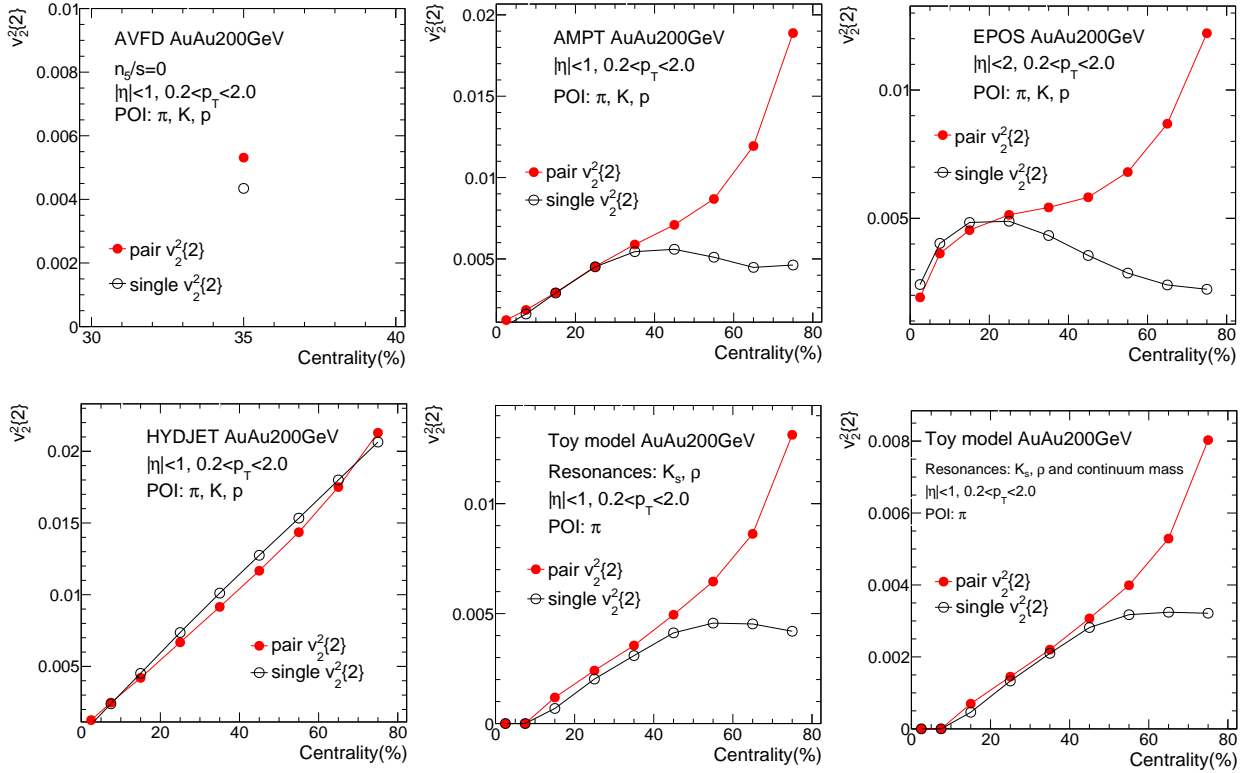


FIG. 4. The average $v_2^2\{2\}$. Shown are the two-particle cumulant $v_2^2\{2\}$ of POIs and $v_{2,\text{pair}}^2\{2\}$ of particle pairs of POIs as functions of centrality from AVFD for $n_5/s = 0$ (upper left), AMPT (upper center), EPOS (upper right), HYDJET (lower left), Toy Model I (lower center), and Toy Model II (lower right). POIs are from acceptances $|\eta| < 1$ and $0.2 < p_T < 2$ GeV/c. The large departure of $v_{2,\text{pair}}^2\{2\}$ from $v_2^2\{2\}$, both calculated by the cumulant method (Eq. 8), is due to self-correlations where two pairs share a common particle. The issue is severe in peripheral collisions except for HYDJET where the average multiplicity is significantly larger than the rest models; for reference, for 30–40% centrality of Au+Au, the average multiplicities are 151, 169, 88, and 255 for AVFD, AMPT, EPOS, and HYDJET, respectively.

in which case the ϕ_1 and ϕ_2 in Eq. 8 are the azimuthal angles of two pairs, each formed by two POIs. Figure 4 shows $v_2\{2\}$ (from 2 POIs) and $v_{2,\text{pair}}\{2\}$ (from 2 pairs of POIs) as functions of centrality in different simulations of Au+Au collisions at $\sqrt{s_{NN}} = 200$ GeV. They roughly agree at high multiplicity (HYDJET, or central collisions of other models), and $v_{2,\text{pair}}\{2\}$ becomes much larger than $v_2\{2\}$ at low multiplicity (peripheral collisions of models except for HYDJET). This discrepancy comes from the autocorrelations where the two pairs share one common POI. To get a feeling of this effect, consider a simplified scenario with $\phi_{\text{pair}} = (\phi_1 + \phi_2)/2$, which is a statistically unbiased assumption. For two pairs with indices (1, 3) and (2, 3) where particle 3 is shared, their correlation is $\cos 2[(\phi_1 + \phi_3)/2 - (\phi_2 + \phi_3)/2] = \cos(\phi_1 - \phi_2)$, and the fraction of this case in the $v_{2,\text{pair}}\{2\}$ calculation is the triplet multiplicity over the quadruplet one, which is $\sim 1/N$. Therefore, besides the common flow component, $v_{2,\text{pair}}\{2\}$ has an extra part $\langle \cos(\phi_1 - \phi_2) \rangle / N$, which accounts qualitatively for its excess over $v_2\{2\}$ when multiplicity is low.

In the ESS method, events are divided into bins of $\hat{q}_{2,\text{pair}}^2$ of equal bin width 0.1. In the ESE method, events are grouped into five ranges in q_2 , four equal size of width 0.5 from $q_2 = 0$ to 2, and the last range $q_2 > 2$. Note this is equivalent to grouping the events according to \hat{q}_2^2 with corresponding divisions.

For the ESS analysis, in each event class according to $\hat{q}_{2,\text{pair}}^2$, we calculate the single particle $v_{2,\text{single}}$ by Eq. 10 and the $\Delta\gamma$ correlator by Eqs. 2,3 using the EP method. The EP azimuthal angle is taken to be $\psi = 0$ as fixed in models. The experimental analogy is data analysis using the first-order event plane reconstructed from spectator neutrons in zero-degree calorimeters (ZDC) [59].

Likewise, in each event class according to \hat{q}_2^2 in the ESE analysis, we also use the known EP of $\psi = 0$ in models to calculate $\langle v_2 \rangle$ by Eq. 10 and $\Delta\gamma$ by Eqs. 2,3. Here, the POI is taken from the west or east subevent in calculating $\langle v_2 \rangle$, and in calculating $\Delta\gamma$, both POIs are taken from either the west subevent or the east subevent. In addition, we use the two-particle cumulant (Eq. 8) to compute $v_2\{2\}$ where one particle is taken from the west subevent and the other from the east subevent, and the three-particle correlator [7] to compute

$$\gamma = \langle \cos(\phi_\alpha + \phi_\beta - 2\phi_c) \rangle / v_2\{2\}, \quad (13)$$

where ϕ_α and ϕ_β are the azimuthal angles of two POIs from the west (east) subevent and ϕ_c is that of a third particle from the other-side subevent, i.e. the east (west) subevent.

IV. RESULTS AND DISCUSSIONS

A. Physics Models

Figure A.1 in the appendix shows AVFD simulation results of $\Delta\gamma$ as functions of $v_{2,\text{single}}$ in bins of $\hat{q}_{2,\text{pair}}^2$ an-

alyzed by the ESS method in 30–40% centrality Au+Au collisions at $\sqrt{s_{NN}} = 200$ GeV. Three values of n_5/s are simulated. The results are consistent with those in Ref. [30]. The intercept at $v_{2,\text{single}} = 0$ is sensitive to CME with v_2 induced background significantly reduced. For $n_5/s = 0$ the intercept is consistent with zero as one would expect if the background is fully removed. For $n_5/s = 0.1$ and 0.2, the intercepts are found to be 1.34×10^{-4} and 5.70×10^{-4} , respectively. The CME signal is expected to scale with $(n_5/s)^2$. The ratio of the ESS intercept for $n_5/s = 0.2$ to that for $n_5/s = 0.1$ is 4.25 ± 0.13 , deviating from the expected ratio of 4 by about 2 standard deviations.

Figure A.2 shows the AVFD results analyzed by the ESE method of $\Delta\gamma$ as functions of v_2 in events classified according to \hat{q}_2^2 from a phase space separated from that of the POIs. Specifically, the \hat{q}_2^2 is calculated using particles from $|\eta| < 0.3$, and the POIs to calculate $\Delta\gamma$ and v_2 are from $0.3 < |\eta| < 2$ (upper cut of 2 instead of typically 1 to increase statistics). The intercept for the $n_5/s = 0$ case is consistent with zero as expected. The intercepts for $n_5/s = 0.1$ and 0.2 are $(1.63 \pm 0.19) \times 10^{-4}$ and $(6.61 \pm 0.19) \times 10^{-4}$, respectively. The statistical uncertainties are larger than those from ESS because of the larger range of projection to the intercept. The intercept ratio between $n_5/s = 0.2$ and 0.1 is 4.06 ± 0.49 , consistent with the expected ratio of 4. It is interesting to note that the fit slopes from both ESS and ESE vary with n_5/s significantly, whereas it is expected to measure the background strength. This is likely because the CME signal is also affecting v_2 of particles in the final state [60] and thus affects the slope as well.

Figure A.3 shows the AMPT results of $\Delta\gamma$ as functions of $v_{2,\text{single}}$ in bins of $\hat{q}_{2,\text{pair}}^2$ analyzed by the ESS method in three centralities of Au+Au collisions at $\sqrt{s_{NN}} = 200$ GeV and 27 GeV. The intercepts are all negative except the 20–30% centrality at 27 GeV which is not statistically significant. Since AMPT does not have CME signals, the results suggest that the ESS intercept may not measure only CME signals but is also sensitive to backgrounds. The fit slope increases with decreasing centrality and is larger at 27 GeV than at 200 GeV; this is expected because the $\Delta\gamma$ background is approximately inversely proportional to multiplicity.

Figure A.4 shows the AMPT results analyzed by the ESE method of $\Delta\gamma$ as functions of v_2 in events classified according to \hat{q}_2^2 (calculated from particles within $|\eta| < 0.3$) from a phase space separated from that of the POIs (taken from $0.3 < |\eta| < 1$). The intercepts are consistent with zero as expected, albeit large statistical uncertainties. The slope fit errors are too large to draw firm conclusions. We have also used \hat{q}_2^2 from particles at forward/backward rapidities $3 < |\eta| < 4$, keeping the same POI acceptance. The results are similar but with larger errors.

Figure A.5 shows the EPOS results of $\Delta\gamma$ as functions of $v_{2,\text{single}}$ in bins of $\hat{q}_{2,\text{pair}}^2$ analyzed by the ESS method in three centralities of Au+Au collisions at $\sqrt{s_{NN}} =$

200 GeV and 27 GeV. The POI and $\hat{q}_{2,\text{pair}}^2$ pseudorapidity acceptance is taken to be $|\eta| < 2$ to increase statistics. The intercepts appear to be positive though with large uncertainties, opposite to those in AMPT. This again suggests that the ESS intercept may be sensitive to backgrounds since EPOS does not have CME signals. There is an indication of an increasing fit slope with decreasing centrality, however, the uncertainties are large.

Figure A.6 shows the EPOS results analyzed by the ESE method of $\Delta\gamma$ as functions of v_2 in events classified according to $\hat{q}_{2,\text{pair}}^2$ from a phase space separated from that of the POIs. The POI pseudorapidity acceptance is taken to be $0.3 < |\eta| < 2$ to increase statistics. The intercepts are consistent with zero as expected, albeit large statistical uncertainties. The slope fit errors are too large to draw firm conclusions.

Figure A.7 shows the HYDJET++ results of $\Delta\gamma$ as functions of $v_{2,\text{single}}$ in bins of $\hat{q}_{2,\text{pair}}^2$ analyzed by the ESS method in three centralities of Au+Au collisions at $\sqrt{s_{NN}} = 200$ GeV and 27 GeV. The intercepts are consistent with zero at 200 GeV but are all positive at 27 GeV. Since HYDJET does not have CME signals, the results again suggest that the ESS intercept may not measure only CME signals but is also sensitive to backgrounds. The HYDJET results further suggest that the degree of the sensitivity of the intercept to backgrounds depends on the collision energy, i.e. details of the event content. The fit slope increases with decreasing centrality and is larger at 27 GeV than at 200 GeV, as expected, similar to the AMPT results.

Figure A.8 shows the HYDJET results analyzed by the ESE method of $\Delta\gamma$ as functions of v_2 in events classified according to $\hat{q}_{2,\text{pair}}^2$ (calculated from particles within $|\eta| < 0.3$) from a phase space separated from that of the POIs (taken from $0.3 < |\eta| < 1$). The intercepts are all consistent with zero as expected, except the 40–50% centrality at 27 GeV where the intercept is displaced from zero but only with less than 2 standard deviations. The fit slope increases with decreasing centrality and is larger at 27 GeV than at 200 GeV, as expected.

We have also used the three-particle correlator method to calculate $\Delta\gamma$ and the two-particle cumulant to calculate $v_2\{2\}$, without relying on the known EP at $\psi = 0$. The results are shown in Fig. A.9 corresponding to the same data in Fig. A.8. The results are consistent with those in Fig. A.8 calculated with the known $\psi = 0$, with somewhat larger statistical uncertainties.

We have also used $\hat{q}_{2,\text{pair}}^2$ from particles at forward/backward pseudorapidities $3 < |\eta| < 4$, keeping the same POI acceptance. The results are shown in Fig. A.10 corresponding to the same data in Fig. A.8. The intercepts are all consistent with zero, except the 30–40% centrality bin at 27 GeV where the intercept is positive away from zero with 2 standard deviations.

B. Discussions on Physics Model Results

We summarize the intercepts and the intercepts divided by the overall $\Delta\gamma$ magnitude from physics model studies by the ESS method in Fig. 5 and by the ESE method in Fig. 6. We observe that the ESS intercepts $\Delta\gamma_{\text{ESS}}$ are close to zero but not always consistent with zero. The ESE intercepts $\Delta\gamma_{\text{ESE}}$ are mostly limited by large statistical uncertainties.

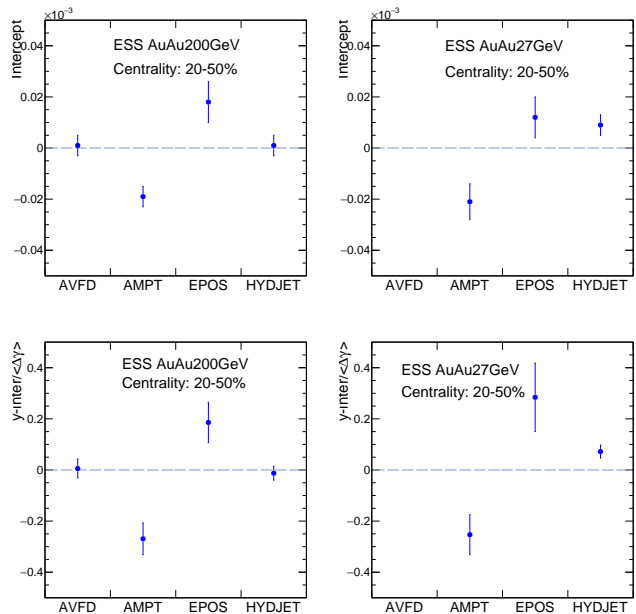


FIG. 5. ESS intercepts. Shown are intercepts (upper panels) and intercept normalized by the inclusive $\Delta\gamma$ magnitude from the ESS method for various physics models. For AVFD ($n_5/s = 0$), the result is from the 30–40% centrality Au+Au collisions at $\sqrt{s_{NN}} = 200$ GeV. For AMPT, EPOS, and HYDJET, the results are from the 20–50% centrality range of Au+Au collisions at $\sqrt{s_{NN}} = 200$ and 27 GeV. The POI η acceptance is $|\eta| < 1$ for AVFD, AMPT, and HYDJET, and $|\eta| < 2$ for EPOS, and the p_T acceptance is $0.2 < p_T < 2$ GeV/c for all models. The $\hat{q}_{2,\text{pair}}^2$ is always calculated from the same POIs.

As discussed in the introduction, the ESS method uses the POIs to compute the event selection $\hat{q}_{2,\text{pair}}^2$ variable. The $\hat{q}_{2,\text{pair}}^2$ is correlated to the $\Delta\gamma$ and $v_{2,\text{single}}$ of POIs and thus selects events based primarily on statistical fluctuations. The wide range of $v_{2,\text{single}}$ and $\Delta\gamma$ are a result of statistical fluctuations by insisting on certain values of $\hat{q}_{2,\text{pair}}^2$. Because of the statistical fluctuation nature, the v_2 -induced backgrounds unnecessarily must be zero in the ESS intercept $\Delta\gamma_{\text{ESS}}$; a model demonstration of this for the similar but simpler ES method can be found in Ref. [34]. It appears from the physics model studies shown in Fig. 5 (where CME is absent) that the value of $\Delta\gamma_{\text{ESS}}$ can be negative, zero, or positive, presumably dependent of model details (described in Sects. III A–III D). On the other hand, it can be proved that the flow-

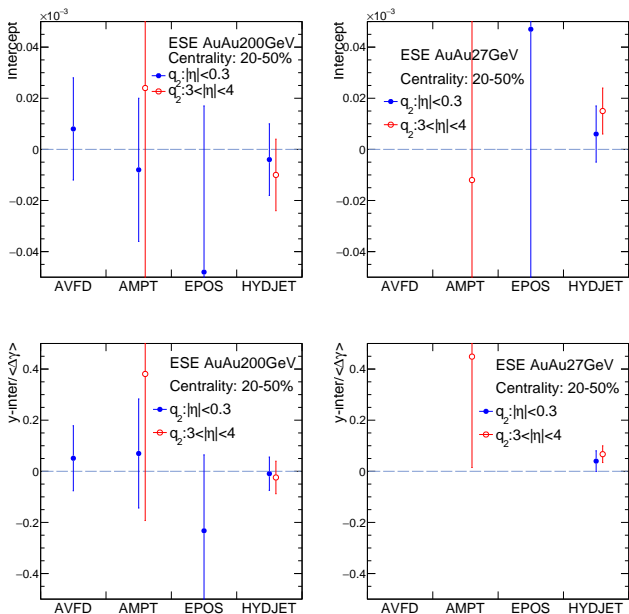


FIG. 6. ESE intercepts. Shown are intercepts (upper panels) and intercept normalized by the inclusive $\Delta\gamma$ magnitude from the ESE method for various physics models. For AVFD ($n_5/s = 0$), the result is from the 30–40% centrality Au+Au collisions at $\sqrt{s_{NN}} = 200$ GeV. For AMPT, EPOS, and HYDJET, the results are from the 20–50% centrality range of Au+Au collisions at $\sqrt{s_{NN}} = 200$ and 27 GeV. The POI η acceptance is $0.3 < |\eta| < 1$ for AVFD, AMPT, and HYDJET, and $0.3 < |\eta| < 2$ for EPOS, and the p_T acceptance is $0.2 < p_T < 2$ GeV/c for all models. The \hat{q}_2^2 is calculated using particles from $|\eta| < 0.3$ for all models (and also $3 < |\eta| < 4$ for AMPT and HYDJET) and $0.2 < p_T < 2$ GeV/c. Several points are missing as they are outside the frame but consistent with zero with large uncertainties.

induced background must be zero at the ESE intercept $\Delta\gamma_{\text{ESE}}$. One thus expects $\Delta\gamma_{\text{ESE}} = 0$ from the studied physics models (where CME is absent) if nonflow is absent (which is the case for results using the known $\psi = 0$). The ESE results are consistent with this expectation as shown in Fig. 6 though the large statistical uncertainties prevent a firm conclusion.

One important difference among the models we studied is the various contributions from K_S . AVFD and AMPT keep the K_S stable so there is no contamination from K_S decay pions in the final state. EPOS and HYDJET, on the other hand, decay K_S so there is maximum contamination of final-state pions (as we have used all pions in the model final state in our calculations). The intercepts from AMPT at both 200 and 27 GeV are negative, and the intercept from AVFD at 200 GeV is consistent with zero (AVFD is not ready for 27 GeV [61]). The intercepts from EPOS at 200 and 27 GeV are both positive. The intercept from HYDJET is consistent with zero at 200 GeV and positive at 27 GeV. In all models the strong-decay resonances (such as the ρ^0 resonance) are forced to de-

cay. Relative particle abundances, for example, the K_S over ρ^0 ratio, depends on energy; the lower the energy, the larger the low- to high-mass ratio. While very much dependent on models, it seems that $\Delta\gamma_{\text{ESS}}$ increases with increasing K_S/ρ^0 ratio. It is thus conceivable, as resonances are a main background contribution to $\Delta\gamma$, that the relative resonance abundances could be important for the ESS intercept.

C. Toy Model Verification

To test the hypothesis that resonance mixtures may influence the robustness of the ESS method, we use toy model simulations, where we can easily alter the event content to examine the consequences. In real data analysis, a fraction of K_S hadrons decay into pions that are reconstructed as primordial particles, often defined experimentally as those with a reconstructed distance of closest approach (DCA) from the reconstructed primary collision point within a certain cut, typically a few centimeters. In the STAR experiment, such a fraction is on the order of 2%, and is used as default in Toy Model I (described in Sect. III E). To alter the event content, we vary the accepted fraction of K_S to 10%, 20%, and 30%.

In addition, we note in Fig. 2 that all the physics models contain a mass continuum of OS pairs in excess of SS pairs. We have therefore included a mass continuum in Toy Model II as described in Sect. III F. The accepted K_S fraction is kept as default. Adding the mass continuum is another way to alter the event content.

Figure A.11 shows the ESS results from Toy Model I (default 2% K_S), Toy Model I (10% K_S), and Toy Model II (mass continuum). It is interesting to notice that the dependence of $\Delta\gamma$ on $v_{2,\text{single}}$ in those $\hat{q}_{2,\text{pair}}^2$ -binned events is not linear for Toy Model II. This suggests that the linear dependence hypothesis, which is essential for the linear extrapolation in ESS, may not be generally valid. Figure A.12 shows the ESE results from Toy Model I (default 2% K_S), Toy Model I (10% K_S), and Toy Model II (mass continuum) with POI's from $0.3 < |\eta| < 1$ and \hat{q}_2^2 from $|\eta| < 0.3$. There seems to be an indication of nonlinear behavior in the Toy Model II results, similar to that in the ESS results in Fig. A.11 right panel. Figure A.13 shows the ESE results from Toy Model I (20% K_S), Toy Model I (30% K_S), and Toy Model II (mass continuum) with POI's from $0.3 < |\eta| < 1$ and \hat{q}_2^2 from forward pseudorapidity region of $3 < |\eta| < 4$, far displaced from that of the POI's.

Figure 7 summarizes the intercepts from the toy model studies. The intercepts from the ESS method appear to be different for the different event contents, verifying our hypothesis that the ESS method is sensitive to the details of the event makeup because of the complex intertwining of the $\Delta\gamma$, $v_{2,\text{single}}$, and the event selection variable $\hat{q}_{2,\text{pair}}^2$.

The intercepts from the ESE method are consistent with zero for the two lower K_S -contamination cases stud-

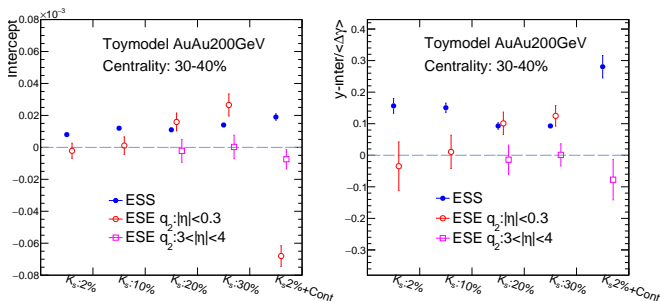


FIG. 7. Toy model ESS and ESE intercepts. Shown are intercepts (left panel) and intercepts normalized by the inclusive $\Delta\gamma$ magnitude (right panel) from the ESS (blue) and ESE (red and pink) methods with the toy models. Toy model inputs are from parameterizations to experimental data of 30–40% Au+Au collisions at 200 GeV. For ESS, the POI acceptance is $|\eta| < 1$ and $0.2 < p_T < 2$ GeV/c, and the $\hat{q}_{2,\text{pair}}^2$ is always calculated from the same POIs. For ESE, the POI acceptance is $0.3 < |\eta| < 1$, and the $\hat{q}_{2,\text{pair}}^2$ is calculated from particles in $|\eta| < 0.3$ (or $3 < |\eta| < 4$ for three of the studied cases), both with $0.2 < p_T < 2$ GeV/c.

ied in Toy Model I. However, it is interesting to notice that the ESE intercepts from the two higher K_S -contamination cases of Toy Model I and the intercept from Toy Model II are inconsistent with zero. We postulate the cause to be nonflow correlations between POI’s in $0.3 < |\eta| < 1$ and the $\hat{q}_{2,\text{pair}}^2$ calculated from $|\eta| < 0.3$ in our toy model studies because resonance-decay daughters can end up in both regions which are not far apart. The effect of adding a mass continuum is different from simply increasing the K_S contamination, presumably because of the differing decay kinematics and opening angles. To reduce nonflow effects, we instead classify events using $\hat{q}_{2,\text{pair}}^2$ calculated from a forward pseudorapidity range far displaced from the POI’s, the ESE intercepts of which are shown in the pink markers in Fig. 7. These intercepts are consistent with zero as expected in the absence of nonflow.

V. SUMMARY

The charge-dependent three-point correlator $\Delta\gamma$ is commonly used to search for the chiral magnetic effect (CME), a parity and charge-parity violating phenomenon predicted by quantum chromodynamics. The $\Delta\gamma$ correlator is contaminated by a major physics background induced by elliptic flow anisotropy v_2 in relativistic heavy ion collisions. The event-shape engineering (ESE) and event-shape selection (ESS) methods have been devised to search for the CME by projecting $\Delta\gamma$ to zero v_2 relying on dynamical fluctuations and statistical fluctuations of v_2 , respectively.

We have conducted a systematic study using four physics models (AVFD, AMPT, EPOS4, and HYD-JET++) describing heavy ion collisions. It is found, with

no CME signal, that the ESS intercept ($\Delta\gamma_{\text{ESS}}$) can be negative, zero, or positive depending on models, and the ESE intercept ($\Delta\gamma_{\text{ESE}}$) is mostly consistent with zero, as expected, albeit inherently large statistical uncertainties.

It is further found, using toy models, that $\Delta\gamma_{\text{ESS}}$ appears to depend on the details of the event content, for example, the relative abundances of resonances and the presence of a mass continuum. Given that the event-shape selection variable $\hat{q}_{2,\text{pair}}^2$, the single particle $v_{2,\text{single}}$, and the three-point correlator $\Delta\gamma$ in $\hat{q}_{2,\text{pair}}^2$ -classified events all depend on the particles of interest (POIs), which are made of not only primordial particles but also all decay products of electromagnetic- and strong-decay resonances and partial products of weak-decay resonances, we conjecture that the ESS intercept $\Delta\gamma_{\text{ESS}}$ is a complicated function of all elements making up the event. These elements include resonance abundances relative to primordial pions, resonance v_2 ’s and p_T spectra, as well as primordial particle v_2 and p_T spectra. One may postulate a diagram such as in Fig. 8 where $\Delta\gamma_{\text{ESS}}$ is depicted as a function of, for the sake of visualization, two elements of the event. For some combinations of the elements, $\Delta\gamma_{\text{ESS}}$ is negative and for some others, $\Delta\gamma_{\text{ESS}}$ is positive; for some lucky combinations, $\Delta\gamma_{\text{ESS}}$ can happen to be zero. The issue is, unfortunately, that it is unknown, needless to say proven, what combinations of all those elements in the event would give the ideal $\Delta\gamma_{\text{ESS}} = 0$ in the absence of CME. This makes it impractical to search for CME using the ESS method.

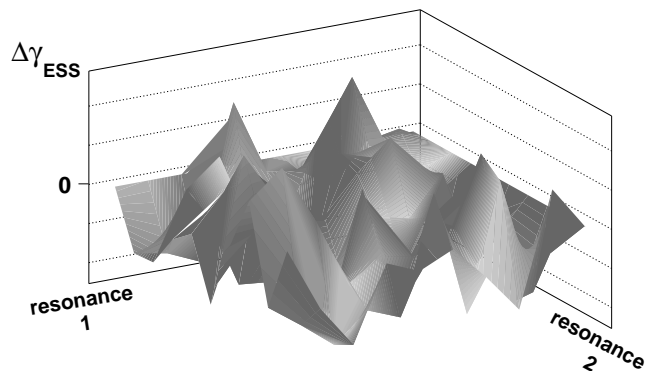


FIG. 8. Postulated behavior (for illustration only) of the ESS intercept $\Delta\gamma_{\text{ESS}}$ on event elements of many dimensions, represented here for visualization purpose only by two, labeled as “resonance 1” and “resonance 2.” In the absence of CME, the value of $\Delta\gamma_{\text{ESS}}$ can be negative or positive, and for some combinations of elements, can happen to be zero. This makes the ESS method a murky and highly model-dependent way for CME searches. This is because of the intertwining $\Delta\gamma$, $v_{2,\text{single}}$, and the event selection variable $\hat{q}_{2,\text{pair}}^2$, all of which are calculated from the same POIs.

The ESE method, on the other side, comes with much more clarity—the intercept of flow-induced backgrounds $\Delta\gamma_{\text{ESE}}$ must be zero. However, the ESE method is not without pitfalls. There exist nonflow correlations be-

tween particles, and when those nonflow correlations are present between POI's and the \hat{q}_2^2 variable classifying events, then the ESE intercept can also be sensitive to non-CME physics. The issue is similar in nature to the ESS method—the relevant variables are now intertwined. One way to avoid/reduce such nonflow effects is to separate POI's and particles to calculate \hat{q}_2^2 well in pseudorapidity. Furthermore, the dynamical fluctuations in v_2 are usually not large enough so that a large extrapolation to the $v_2 = 0$ intercept is needed in the ESE method. This results in a relatively large uncertainty

in the extrapolated intercept, and large statistics are required for precision measurement by the ESE method. The statistics issue, however, can easily be resolved, at least conceptually, by accumulating more data.

ACKNOWLEDGMENT

This work is supported in part by the U.S. Department of Energy (Grant No. DE-SC0012910).

-
- [1] D. Kharzeev, R. Pisarski, and M. H. Tytgat, Possibility of spontaneous parity violation in hot QCD, *Phys.Rev.Lett.* **81**, 512 (1998), arXiv:hep-ph/9804221 [hep-ph].
- [2] D. Kharzeev, Parity violation in hot QCD: Why it can happen, and how to look for it, *Phys.Lett.* **B633**, 260 (2006), arXiv:hep-ph/0406125 [hep-ph].
- [3] D. E. Kharzeev, L. D. McLerran, and H. J. Warringa, The Effects of topological charge change in heavy ion collisions: 'Event by event P and CP violation', *Nucl.Phys.* **A803**, 227 (2008), arXiv:0711.0950 [hep-ph].
- [4] K. Fukushima, D. E. Kharzeev, and H. J. Warringa, The chiral magnetic effect, *Phys.Rev.* **D78**, 074033 (2008), arXiv:0808.3382 [hep-ph].
- [5] V. Skokov, A. Yu. Illarionov, and V. Toneev, Estimate of the magnetic field strength in heavy-ion collisions, *Int. J. Mod. Phys.* **A24**, 5925 (2009), arXiv:0907.1396 [nucl-th].
- [6] W.-T. Deng and X.-G. Huang, Event-by-event generation of electromagnetic fields in heavy-ion collisions, *Phys. Rev.* **C85**, 044907 (2012), arXiv:1201.5108 [nucl-th].
- [7] S. A. Voloshin, Parity violation in hot QCD: How to detect it, *Phys.Rev.* **C70**, 057901 (2004), arXiv:hep-ph/0406311 [hep-ph].
- [8] U. Heinz and R. Snellings, Collective flow and viscosity in relativistic heavy-ion collisions, *Ann.Rev.Nucl.Part.Sci.* **63**, 123 (2013), arXiv:1301.2826 [nucl-th].
- [9] D. E. Kharzeev, J. Liao, S. A. Voloshin, and G. Wang, Chiral magnetic and vortical effects in high-energy nuclear collisions—A status report, *Prog. Part. Nucl. Phys.* **88**, 1 (2016), arXiv:1511.04050 [hep-ph].
- [10] B. Abelev *et al.* (STAR Collaboration), Azimuthal Charged-Particle Correlations and Possible Local Strong Parity Violation, *Phys.Rev.Lett.* **103**, 251601 (2009), arXiv:0909.1739 [nucl-ex].
- [11] B. Abelev *et al.* (STAR Collaboration), Observation of charge-dependent azimuthal correlations and possible local strong parity violation in heavy ion collisions, *Phys.Rev.* **C81**, 054908 (2010), arXiv:0909.1717 [nucl-ex].
- [12] B. Abelev *et al.* (ALICE), Charge separation relative to the reaction plane in Pb-Pb collisions at $\sqrt{s_{NN}} = 2.76$ TeV, *Phys.Rev.Lett.* **110**, 012301 (2013), arXiv:1207.0900 [nucl-ex].
- [13] J. Zhao, Search for the Chiral Magnetic Effect in Relativistic Heavy-Ion Collisions, *Int. J. Mod. Phys.* **A33**, 1830010 (2018), arXiv:1805.02814 [nucl-ex].
- [14] F. Wang, Effects of Cluster Particle Correlations on Local Parity Violation Observables, *Phys.Rev.* **C81**, 064902 (2010), arXiv:0911.1482 [nucl-ex].
- [15] J. Liao, V. Koch, and A. Bzdak, On the Charge Separation Effect in Relativistic Heavy Ion Collisions, *Phys.Rev.* **C82**, 054902 (2010), arXiv:1005.5380 [nucl-th].
- [16] S. Schlichting and S. Pratt, Charge conservation at energies available at the BNL Relativistic Heavy Ion Collider and contributions to local parity violation observables, *Phys.Rev.* **C83**, 014913 (2011), arXiv:1009.4283 [nucl-th].
- [17] J. Zhao and F. Wang, Experimental searches for the chiral magnetic effect in heavy-ion collisions, *Prog. Part. Nucl. Phys.* **107**, 200 (2019), arXiv:1906.11413 [nucl-ex].
- [18] L. Adamczyk *et al.* (STAR), Measurement of charge multiplicity asymmetry correlations in high-energy nucleus-nucleus collisions at $\sqrt{s_{NN}} = 200$ GeV, *Phys. Rev.* **C89**, 044908 (2014), arXiv:1303.0901 [nucl-ex].
- [19] L. Adamczyk *et al.* (STAR), Beam-energy dependence of charge separation along the magnetic field in Au+Au collisions at RHIC, *Phys. Rev. Lett.* **113**, 052302 (2014), arXiv:1404.1433 [nucl-ex].
- [20] V. Khachatryan *et al.* (CMS), Observation of charge-dependent azimuthal correlations in p -Pb collisions and its implication for the search for the chiral magnetic effect, *Phys. Rev. Lett.* **118**, 122301 (2017), arXiv:1610.00263 [nucl-ex].
- [21] J. Adam *et al.* (STAR), Charge-dependent pair correlations relative to a third particle in $p + Au$ and $d + Au$ collisions at RHIC, *Phys. Lett.* **B798**, 134975 (2019), arXiv:1906.03373 [nucl-ex].
- [22] S. Acharya *et al.* (ALICE), Constraining the Chiral Magnetic Effect with charge-dependent azimuthal correlations in Pb-Pb collisions at $\sqrt{s_{NN}} = 2.76$ and 5.02 TeV, *JHEP* **09**, 160, arXiv:2005.14640 [nucl-ex].
- [23] S. Acharya *et al.* (ALICE), Constraining the magnitude of the Chiral Magnetic Effect with Event Shape Engineering in Pb-Pb collisions at $\sqrt{s_{NN}} = 2.76$ TeV, *Phys. Lett.* **B777**, 151 (2018), arXiv:1709.04723 [nucl-ex].
- [24] A. M. Sirunyan *et al.* (CMS), Constraints on the chiral magnetic effect using charge-dependent azimuthal correlations in pPb and $PbPb$ collisions at the CERN Large Hadron Collider, *Phys. Rev.* **C97**, 044912 (2018), arXiv:1708.01602 [nucl-ex].
- [25] H.-J. Xu, J. Zhao, X. Wang, H. Li, Z.-W. Lin, C. Shen, and F. Wang, Varying the chiral magnetic effect relative to flow in a single nucleus-nucleus collision, *Chin. Phys.* **C42**, 084103 (2018), arXiv:1710.07265 [nucl-th].
- [26] S. A. Voloshin, Estimate of the signal from the chiral magnetic effect in heavy-ion collisions from measurements relative to the participant and specta-

- tor flow planes, *Phys. Rev. C* **98**, 054911 (2018), [arXiv:1805.05300 \[nucl-ex\]](#).
- [27] M. Abdallah *et al.* (STAR), Search for the Chiral Magnetic Effect via Charge-Dependent Azimuthal Correlations Relative to Spectator and Participant Planes in Au+Au Collisions at $\sqrt{s_{NN}} = 200$ GeV, *Phys. Rev. Lett.* **128**, 092301 (2022), [arXiv:2106.09243 \[nucl-ex\]](#).
- [28] S. Choudhury *et al.*, Investigation of experimental observables in search of the chiral magnetic effect in heavy-ion collisions in the STAR experiment, *Chin. Phys. C* **46**, 014101 (2022), [arXiv:2105.06044 \[nucl-ex\]](#).
- [29] J. Schukraft, A. Timmins, and S. A. Voloshin, Ultra-relativistic nuclear collisions: event shape engineering, *Phys. Lett. B* **719**, 394 (2013), [arXiv:1208.4563 \[nucl-ex\]](#).
- [30] Z. Xu, B. Chan, G. Wang, A. Tang, and H. Z. Huang, Event shape selection method in search of the chiral magnetic effect in heavy-ion collisions, *Phys. Lett. B* **848**, 138367 (2024), [arXiv:2307.14997 \[nucl-th\]](#).
- [31] A. M. Poskanzer and S. Voloshin, Methods for analyzing anisotropic flow in relativistic nuclear collisions, *Phys. Rev. C* **58**, 1671 (1998), [arXiv:nucl-ex/9805001 \[nucl-ex\]](#).
- [32] R. S. Bhalerao and J.-Y. Ollitrault, Eccentricity fluctuations and elliptic flow at RHIC, *Phys. Lett. B* **641**, 260 (2006), [arXiv:nucl-th/0607009 \[nucl-th\]](#).
- [33] Y. Feng, J. Zhao, H. Li, H.-j. Xu, and F. Wang, Two- and three-particle nonflow contributions to the chiral magnetic effect measurement by spectator and participant planes in relativistic heavy ion collisions, *Phys. Rev. C* **105**, 024913 (2022), [arXiv:2106.15595 \[nucl-ex\]](#).
- [34] F. Wang and J. Zhao, Challenges in flow background removal in search for the chiral magnetic effect, *Phys. Rev. C* **95**, 051901 (2017), [arXiv:1608.06610 \[nucl-th\]](#).
- [35] B. Abelev *et al.* (STAR Collaboration), Systematic measurements of identified particle spectra in *pp*, *d*+Au and Au+Au collisions from STAR, *Phys. Rev. C* **79**, 034909 (2009), [arXiv:0808.2041 \[nucl-ex\]](#).
- [36] S. Shi, Y. Jiang, E. Lilleskov, and J. Liao, Anomalous Chiral Transport in Heavy Ion Collisions from Anomalous-Viscous Fluid Dynamics, *Annals Phys.* **394**, 50 (2018), [arXiv:1711.02496 \[nucl-th\]](#).
- [37] Y. Jiang, S. Shi, Y. Yin, and J. Liao, Quantifying the chiral magnetic effect from anomalous-viscous fluid dynamics, *Chin. Phys. C* **42**, 011001 (2018), [arXiv:1611.04586 \[nucl-th\]](#).
- [38] S. Shi, H. Zhang, D. Hou, and J. Liao, Signatures of Chiral Magnetic Effect in the Collisions of Isobars, *Phys. Rev. Lett.* **125**, 242301 (2020), [arXiv:1910.14010 \[nucl-th\]](#).
- [39] U. W. Heinz and J. Liu, Pre-equilibrium dynamics and heavy-ion observables, *Nucl. Phys. A* **956**, 549 (2016), [arXiv:1512.08276 \[nucl-th\]](#).
- [40] J. Błoczyński, X.-G. Huang, X. Zhang, and J. Liao, Azimuthally fluctuating magnetic field and its impacts on observables in heavy-ion collisions, *Phys. Lett. B* **718**, 1529 (2013), [arXiv:1209.6594 \[nucl-th\]](#).
- [41] Z.-W. Lin, C. M. Ko, B.-A. Li, B. Zhang, and S. Pal, A Multi-phase transport model for relativistic heavy ion collisions, *Phys. Rev. C* **72**, 064901 (2005), [arXiv:nucl-th/0411110 \[nucl-th\]](#).
- [42] M. Gyulassy and X.-N. Wang, HIJING 1.0: A Monte Carlo program for parton and particle production in high-energy hadronic and nuclear collisions, *Comput. Phys. Commun.* **83**, 307 (1994), [arXiv:nucl-th/9502021 \[nucl-th\]](#).
- [43] Z.-W. Lin and C. Ko, Partonic effects on the elliptic flow at RHIC, *Phys. Rev. C* **65**, 034904 (2002), [arXiv:nucl-th/0108039 \[nucl-th\]](#).
- [44] B. Zhang, ZPC 1.0.1: A Parton cascade for ultrarelativistic heavy ion collisions, *Comput. Phys. Commun.* **109**, 193 (1998), [arXiv:nucl-th/9709009 \[nucl-th\]](#).
- [45] K. Werner, Revealing a deep connection between factorization and saturation: New insight into modeling high-energy proton-proton and nucleus-nucleus scattering in the EPOS4 framework, *Phys. Rev. C* **108**, 064903 (2023), [arXiv:2301.12517 \[hep-ph\]](#).
- [46] K. Werner and B. Guiot, Perturbative QCD concerning light and heavy flavor in the EPOS4 framework, *Phys. Rev. C* **108**, 034904 (2023), [arXiv:2306.02396 \[hep-ph\]](#).
- [47] K. Werner, Parallel scattering, saturation, and generalized Abramovskii-Gribov-Kancheli (AGK) theorem in the EPOS4 framework, with applications for heavy-ion collisions at sNN of 5.02 TeV and 200 GeV, *Phys. Rev. C* **109**, 034918 (2024), [arXiv:2310.09380 \[hep-ph\]](#).
- [48] K. Werner, Core-corona procedure and microcanonical hadronization to understand strangeness enhancement in proton-proton and heavy ion collisions in the EPOS4 framework, *Phys. Rev. C* **109**, 014910 (2024), [arXiv:2306.10277 \[hep-ph\]](#).
- [49] I. P. Lokhtin, A. V. Belyaev, L. V. Malinina, S. V. Petrushanko, E. P. Rogochaya, and A. M. Snigirev, Hadron spectra, flow and correlations in PbPb collisions at the LHC: interplay between soft and hard physics, *Eur. Phys. J. C* **72**, 2045 (2012), [arXiv:1204.4820 \[hep-ph\]](#).
- [50] L. V. Bravina, B. H. Bruschheim Johansson, G. K. Eyyubova, V. L. Korotkikh, I. P. Lokhtin, L. V. Malinina, S. V. Petrushanko, A. M. Snigirev, and E. E. Zabrodin, Higher harmonics of azimuthal anisotropy in relativistic heavy ion collisions in HYDJET++ model, *Eur. Phys. J. C* **74**, 2807 (2014), [arXiv:1311.7054 \[nucl-th\]](#).
- [51] T. Sjostrand, P. Eden, C. Friberg, L. Lonnblad, G. Miu, *et al.*, High-energy physics event generation with PYTHIA 6.1, *Comput. Phys. Commun.* **135**, 238 (2001), [arXiv:hep-ph/0010017 \[hep-ph\]](#).
- [52] K. A. Olive *et al.* (Particle Data Group), Review of Particle Physics, *Chin. Phys. C* **38**, 090001 (2014).
- [53] J. Adams *et al.* (STAR), Rho0 production and possible modification in Au+Au and p+p collisions at $S(NN)^{1/2} = 200$ -GeV, *Phys. Rev. Lett.* **92**, 092301 (2004), [arXiv:nucl-ex/0307023](#).
- [54] L. Adamczyk *et al.* (STAR), Measurements of Dielectron Production in Au+Au Collisions at $\sqrt{s_{NN}} = 200$ GeV from the STAR Experiment, *Phys. Rev. C* **92**, 024912 (2015), [arXiv:1504.01317 \[hep-ex\]](#).
- [55] S. S. Adler *et al.* (PHENIX), Suppressed π^0 production at large transverse momentum in central Au+Au collisions at $\sqrt{s_{NN}} = 200$ GeV, *Phys. Rev. Lett.* **91**, 072301 (2003), [arXiv:nucl-ex/0304022](#).
- [56] J. Adams *et al.* (STAR), Identified particle distributions in pp and Au+Au collisions at $s(NN)^{1/2} = 200$ GeV, *Phys. Rev. Lett.* **92**, 112301 (2004), [arXiv:nucl-ex/0310004](#).
- [57] X. Dong, S. Esumi, P. Sorensen, N. Xu, and Z. Xu, Resonance decay effects on anisotropy parameters, *Phys. Lett. B* **597**, 328 (2004), [arXiv:nucl-th/0403030](#).
- [58] K. Ackermann *et al.* (STAR Collaboration), STAR detector overview, *Nucl. Instrum. Meth.* **A499**, 624 (2003).

- [59] C. Adler *et al.*, The RHIC zero-degree calorimeters, [Nucl.Instrum.Meth. **A499**, 433 \(2003\)](#).
- [60] H.-S. Li, Y. Feng, and F. Wang, Influence of the chiral magnetic effect on particle-pair elliptic anisotropy (2024), [arXiv:2404.05032 \[hep-ph\]](#).
- [61] J. Liao, private communications.

Appendix A: Simulation Plots

This appendix compiles all simulation plots of $\Delta\gamma$ as functions of v_2 analyzed by the ESS and ESE methods from physics models as well as from toy models.

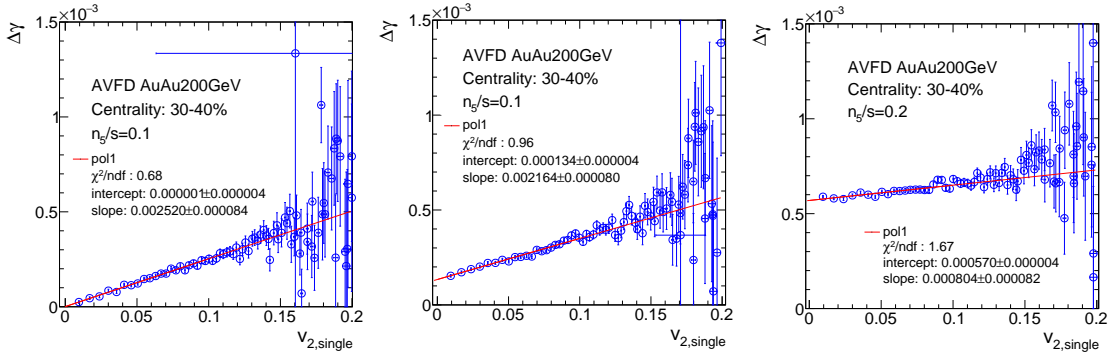


FIG. A.1. AVFD ESS results. Three values of $n_5/s = 0$ (left panel), 0.1 (center panel), and 0.2 (right panel) are implemented in the AVFD simulations of Au+Au collisions at $\sqrt{s_{NN}} = 200$ GeV, with approximately 2×10^7 events each for the 30–40% centrality. The $\Delta\gamma$ is plotted as a function of $v_{2,\text{single}}$ in events binned in $\hat{q}_{2,\text{pair}}^2\{2\}$ (Eqs. 5,9). POIs are from acceptance $|\eta| < 1$ and $0.2 < p_T < 2$ GeV/c, and the event selection variable $\hat{q}_{2,\text{pair}}^2\{2\}$ is computed from the same POIs. The model's known impact parameter direction $\psi = 0$ is taken as the EP in calculating $\Delta\gamma$ (Eqs. 2,3) and $v_{2,\text{single}}$ (Eq. 10).

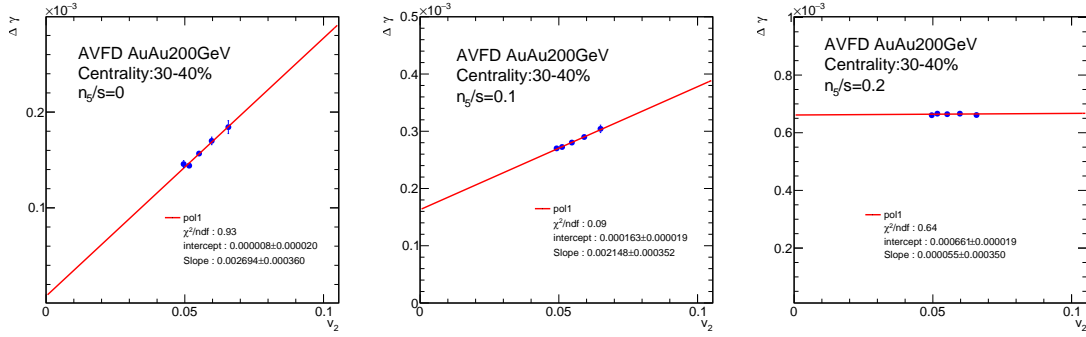


FIG. A.2. AVFD ESE results. Three values of $n_5/s = 0$ (left panel), 0.1 (center panel), and 0.2 (right panel) are implemented in the AVFD simulations of Au+Au collisions at $\sqrt{s_{NN}} = 200$ GeV, with approximately 2×10^7 events each for the 30–40% centrality. The $\Delta\gamma$ is plotted as a function of v_2 in events binned in $\hat{q}_2^2\{2\}$ (Eqs. 5,6). POIs are from acceptance $0.3 < |\eta| < 2$, and the event selection variable $\hat{q}_2^2\{2\}$ is computed from particles in $|\eta| < 0.3$, both with $0.2 < p_T < 2$ GeV/c. The model's known impact parameter direction $\psi = 0$ is taken as the EP in calculating $\Delta\gamma$ (Eqs. 2,3) and $\langle v_2 \rangle$ (Eq. 10).

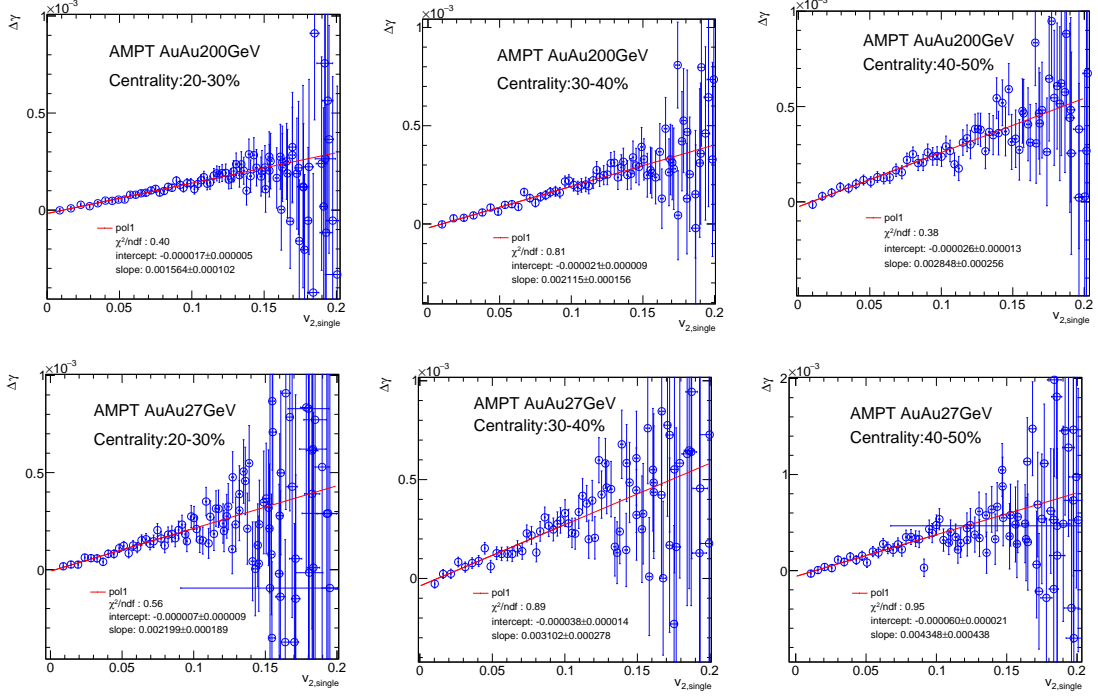


FIG. A.3. AMPT ESS results. Shown are three centralities of Au+Au collisions at $\sqrt{s_{NN}} = 200$ GeV (upper panels) and at 27 GeV (lower panels) simulated by AMPT, with approximately 5×10^6 events for each centrality at each energy. The $\Delta\gamma$ is plotted as a function of $v_{2,\text{single}}$ in events binned in $q_2^2\{2\}$ (Eqs. 5,9). POIs are from acceptance $|\eta| < 1$ and $0.2 < p_T < 2$ GeV/c, and the event selection variable $\hat{q}_2^2\{2\}$ is computed from the same POIs. The model's known impact parameter direction $\psi = 0$ is taken as the EP in calculating $\Delta\gamma$ (Eqs. 2,3) and $v_{2,\text{single}}$ (Eq. 10).

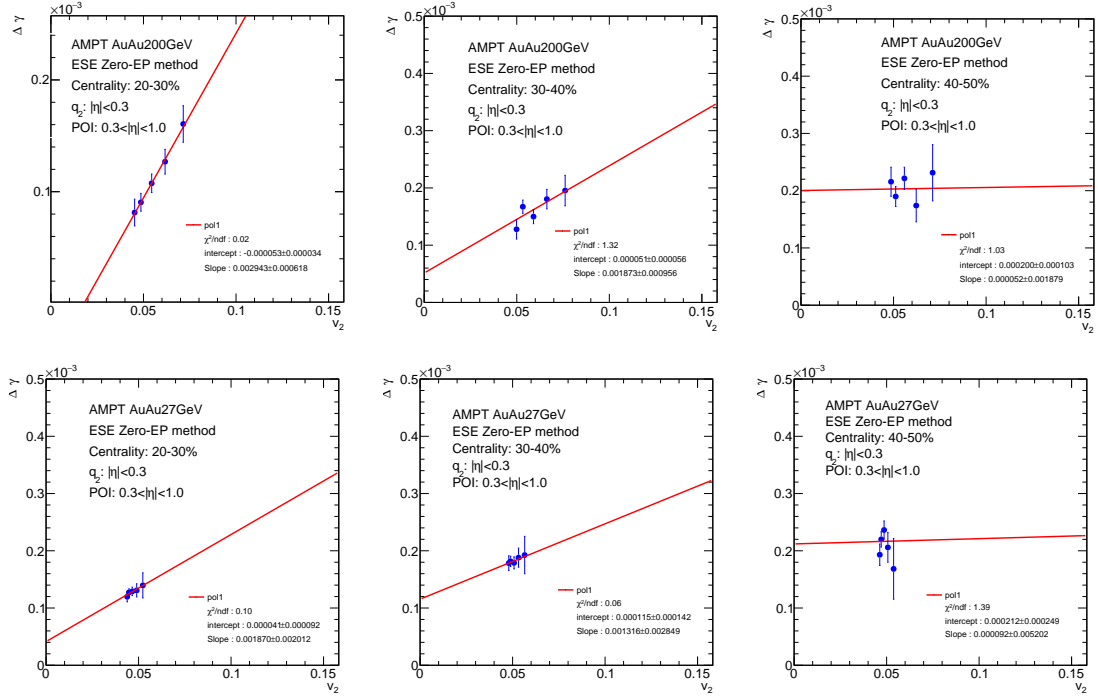


FIG. A.4. AMPT ESE results. Shown are three centralities of Au+Au collisions at $\sqrt{s_{NN}} = 200$ GeV (upper panels) and at 27 GeV (lower panels) simulated by AMPT, with approximately 5×10^6 events for each centrality at each energy. The $\Delta\gamma$ is plotted as a function of v_2 in events binned in $q_2^2\{2\}$ (Eqs. 5,6). POIs are from acceptance $0.3 < |\eta| < 1$, and the event selection variable $\hat{q}_2^2\{2\}$ is computed from particles in $|\eta| < 0.3$, both with $0.2 < p_T < 2$ GeV/c. The model's known impact parameter direction $\psi = 0$ is taken as the EP in calculating $\Delta\gamma$ (Eqs. 2,3) and $\langle v_2 \rangle$ (Eq. 10).

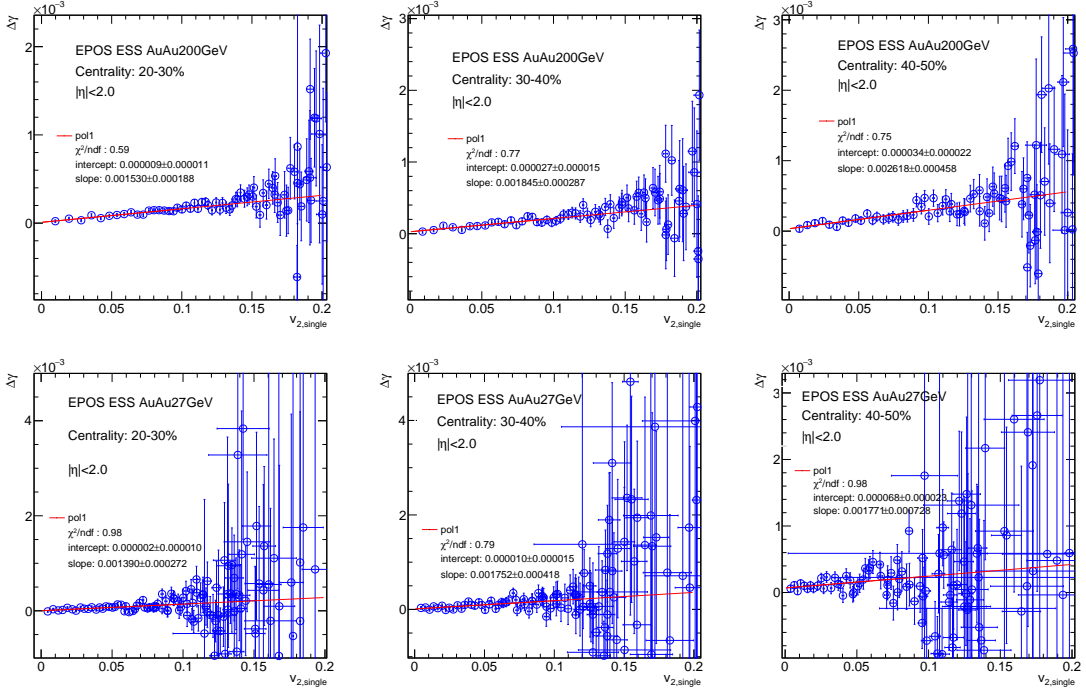


FIG. A.5. EPOS ESS results. Shown are three centralities of Au+Au collisions at $\sqrt{s_{NN}} = 200$ GeV (upper panels) and at 27 GeV (lower panels) simulated by EPOS4, with approximately 1.6×10^6 and 8×10^5 events for each centrality, respectively. The $\Delta\gamma$ is plotted as a function of $v_{2,single}$ in events binned in $\hat{q}_{2,pair}^2\{2\}$ (Eqs. 5,9). POIs are from acceptance $|\eta| < 2$ and $0.2 < p_T < 2$ GeV/c, and the event selection variable $\hat{q}_{2,pair}^2\{2\}$ is computed from the same POIs. The model's known impact parameter direction $\psi = 0$ is taken as the EP in calculating $\Delta\gamma$ (Eqs. 2,3) and $v_{2,single}$ (Eq. 10).

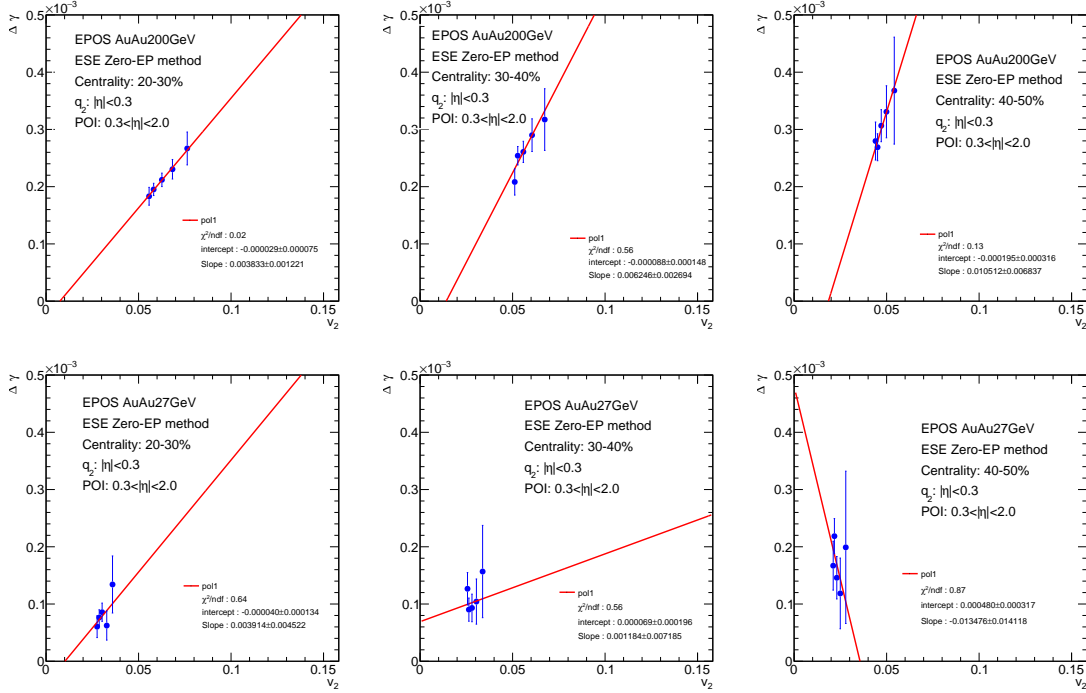


FIG. A.6. EPOS ESE results. Shown are three centralities of Au+Au collisions at $\sqrt{s_{NN}} = 200$ GeV (upper panels) and at 27 GeV (lower panels) simulated by EPOS4, with approximately 1.6×10^6 and 8×10^5 events for each centrality, respectively. The $\Delta\gamma$ is plotted as a function of v_2 in events binned in $\hat{q}_2^2\{2\}$ (Eqs. 5,6). POIs are from acceptance $0.3 < |\eta| < 2$ and $0.2 < p_T < 2$ GeV/c, and the event selection variable $\hat{q}_2^2\{2\}$ is computed from particles in $|\eta| < 0.3$, both with $0.2 < p_T < 2$ GeV/c. The model's known impact parameter direction $\psi = 0$ is taken as the EP in calculating $\Delta\gamma$ (Eqs. 2,3) and $\langle v_2 \rangle$ (Eq. 10).

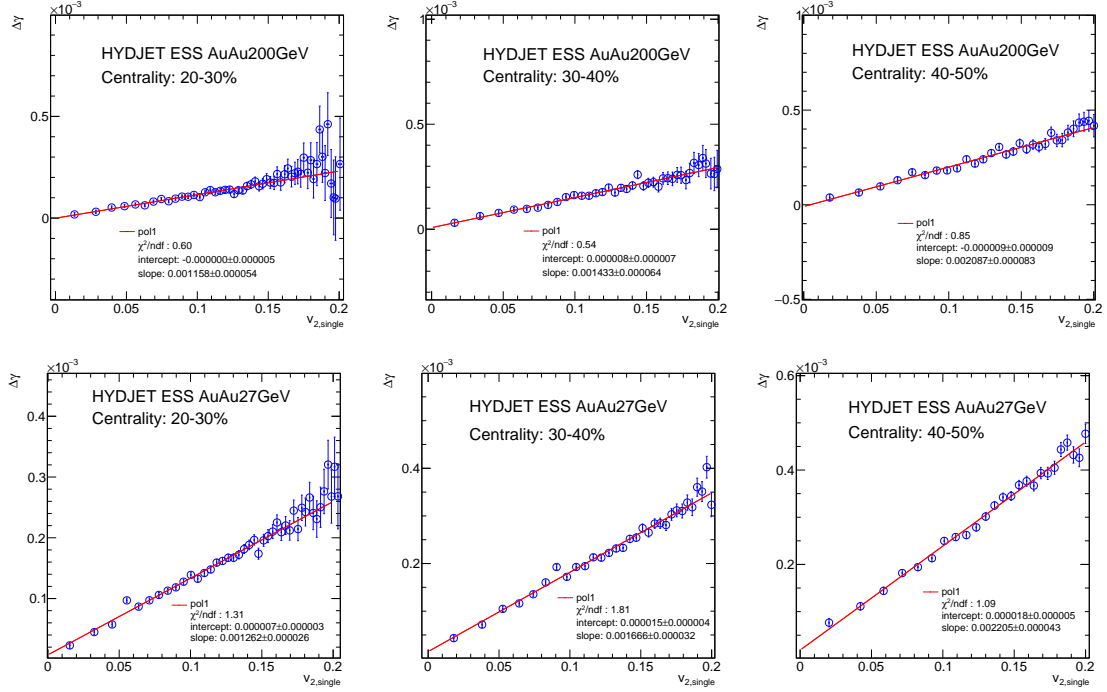


FIG. A.7. HYDJET++ ESS results. Shown are three centralities of Au+Au collisions at $\sqrt{s_{NN}} = 200$ GeV (upper panels) and at 27 GeV (lower panels) simulated by HYDJET++, with approximately 4×10^6 and 10^7 events for each centrality, respectively. The $\Delta\gamma$ is plotted as a function of $v_{2,\text{single}}$ in events binned in $\hat{q}_2^2\{2\}$ (Eqs. 5,9). POIs are from acceptance $|\eta| < 1$ and $0.2 < p_T < 2$ GeV/c, and the event selection variable $\hat{q}_2^2\{2\}$ is computed from the same POIs. The model's known impact parameter direction $\psi = 0$ is taken as the EP in calculating $\Delta\gamma$ (Eqs. 2,3) and $v_{2,\text{single}}$ (Eq. 10).

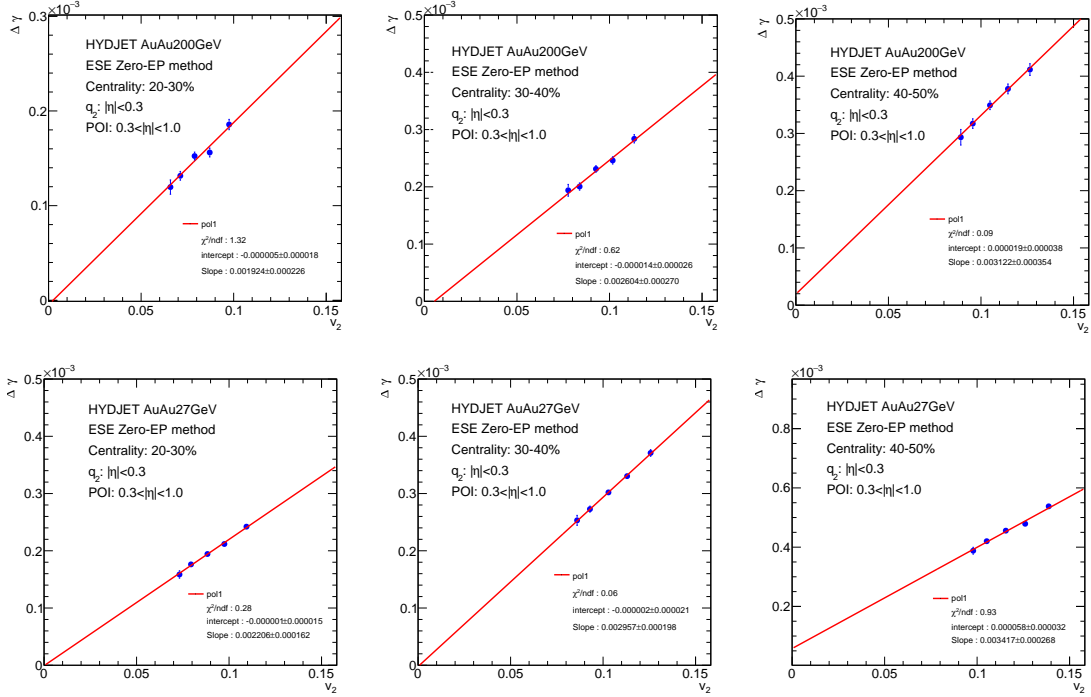


FIG. A.8. HYDJET++ ESE results. Shown are three centralities of Au+Au collisions at $\sqrt{s_{NN}} = 200$ GeV (upper panels) and at 27 GeV (lower panels) simulated by HYDJET++, with approximately 4×10^6 and 10^7 events for each centrality, respectively. The $\Delta\gamma$ is plotted as a function of v_2 in events binned in $\hat{q}_2^2\{2\}$ (Eqs. 5,6). POIs are from acceptance $0.3 < |\eta| < 1$ and $0.2 < p_T < 2$ GeV/c, and the event selection variable $\hat{q}_2^2\{2\}$ is computed from particles in $|\eta| < 0.3$, both with $0.2 < p_T < 2$ GeV/c. The model's known impact parameter direction $\psi = 0$ is taken as the EP in calculating $\Delta\gamma$ (Eqs. 2,3) and $\langle v_2 \rangle$ (Eq. 10).

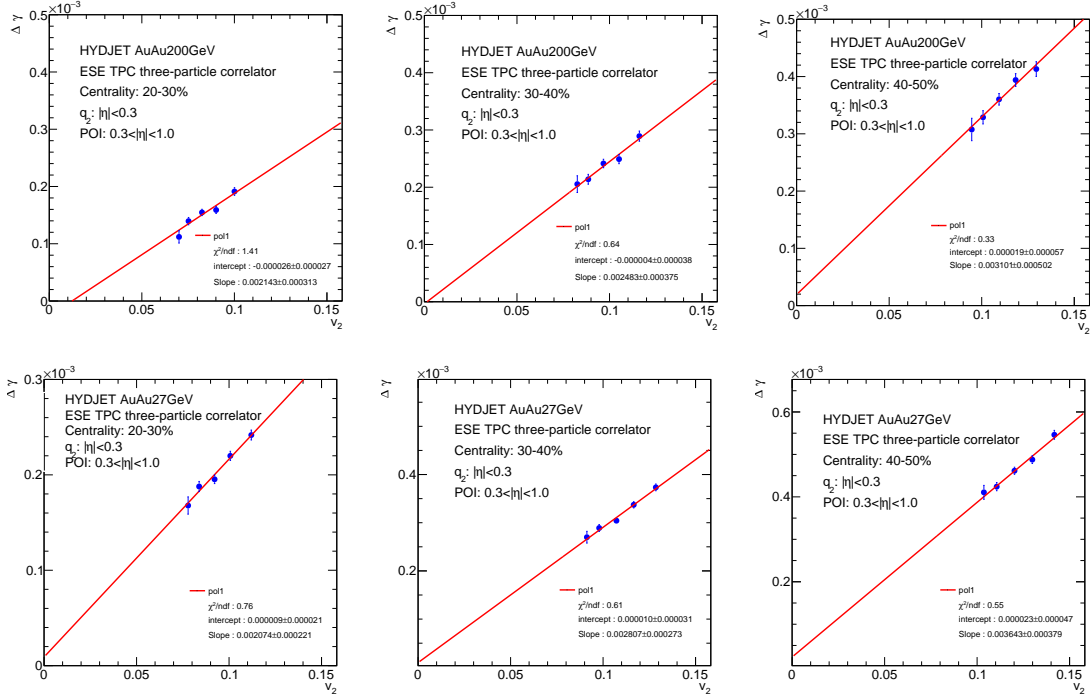


FIG. A.9. HYDJET++ ESE results (three-particle correlator). Shown are three centralities of Au+Au collisions at $\sqrt{s_{NN}} = 200$ GeV (upper panels) and at 27 GeV (lower panels) simulated by HYDJET++, with approximately 4×10^6 and 10^7 events for each centrality, respectively. The $\Delta\gamma$ is plotted as a function of v_2 in events binned in $\hat{q}_2^2\{2\}$ (Eqs. 5,6). POIs are from acceptance $0.3 < |\eta| < 1$, and the event selection variable $\hat{q}_2^2\{2\}$ is computed from particles in $|\eta| < 0.3$, both with $0.2 < p_T < 2$ GeV/c. The three-particle correlator method is used to calculate $\Delta\gamma$ (Eq. 13) and the two-particle cumulant is used to calculate $\langle v_2 \rangle$ (Eq. 8).

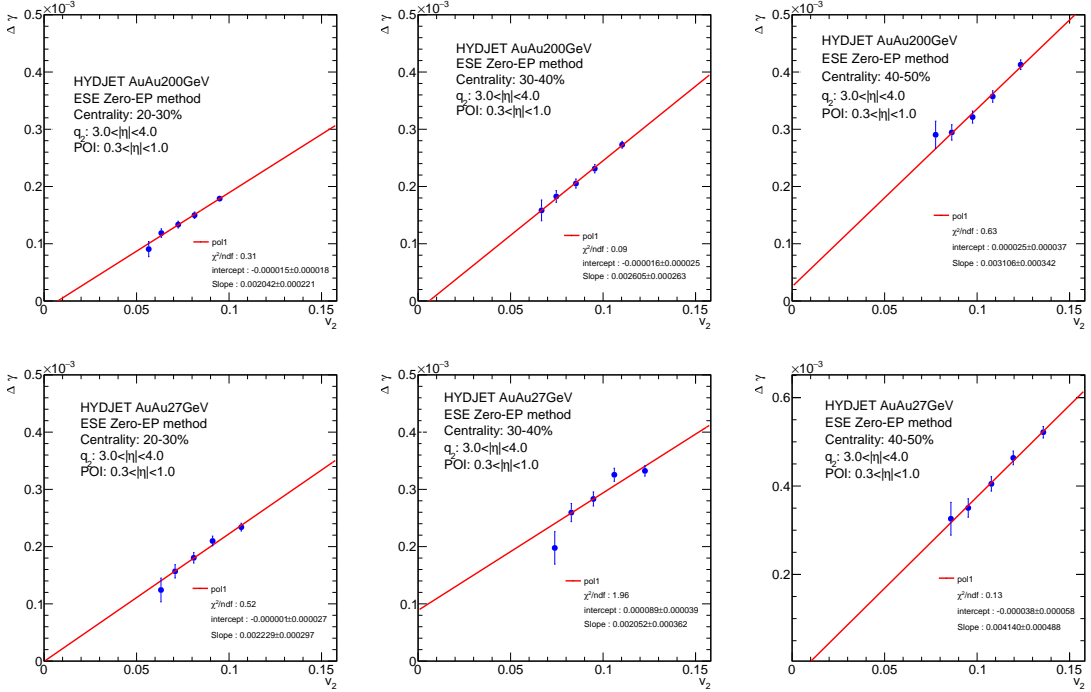


FIG. A.10. HYDJET++ ESE results (forward/backward rapidity \hat{q}_2^2). Shown are three centralities of Au+Au collisions at $\sqrt{s_{NN}} = 200$ GeV (upper panels) and at 27 GeV (lower panels) simulated by HYDJET++, with approximately 4×10^6 and 10^7 events for each centrality, respectively. The $\Delta\gamma$ is plotted as a function of v_2 in events binned in $\hat{q}_2^2\{2\}$. POIs are from acceptance $0.3 < |\eta| < 1$, and the event selection variable $\hat{q}_2^2\{2\}$ (Eqs. 5,6) is computed from particles in forward/backward pseudorapidity regions of $3 < |\eta| < 4$, both with $0.2 < p_T < 2$ GeV/c. The model's known impact parameter direction $\psi = 0$ is taken as the EP in calculating $\Delta\gamma$ by Eqs. (2,3) and $\langle v_2 \rangle$ by Eq. (10).

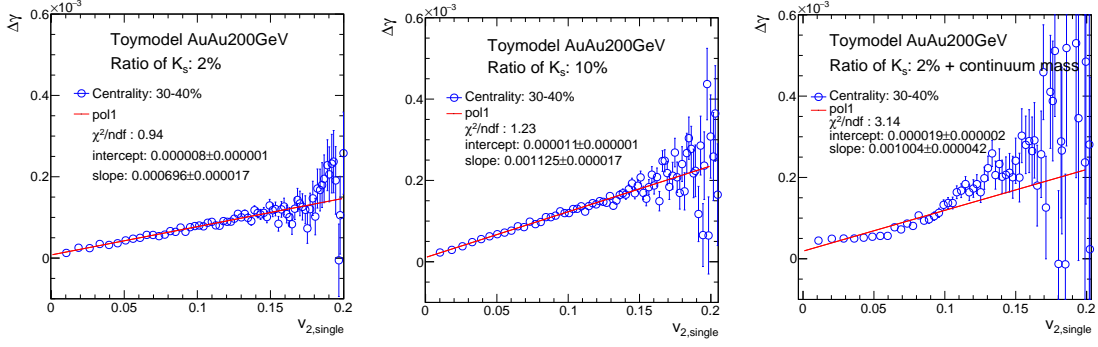


FIG. A.11. Toy model ESS results. Toy Model I with the accepted K_S fraction of the default 2% (left panel) and of 10% (middle panel), and Toy Model II with mass continuum (right panel). The K_S , ρ^0 , and primordial pion inputs are from parameterizations to experimental data of 30–40% centrality Au+Au collisions at $\sqrt{s_{NN}} = 200$ GeV. The numbers of events are 2×10^8 for each panel. The $\Delta\gamma$ is plotted as a function of $v_{2,\text{single}}$ in events binned in $\hat{q}_2^2\{2\}$ (Eqs. 5,9). POIs are from acceptance $|\eta| < 1$ and $0.2 < p_T < 2$ GeV/c, and the event selection variable $\hat{q}_2^2\{2\}$ is computed from the same POIs. The model's known impact parameter direction $\psi = 0$ is taken as the EP in calculating $\Delta\gamma$ (Eqs. 2,3) and $v_{2,\text{single}}$ (Eq. 10).

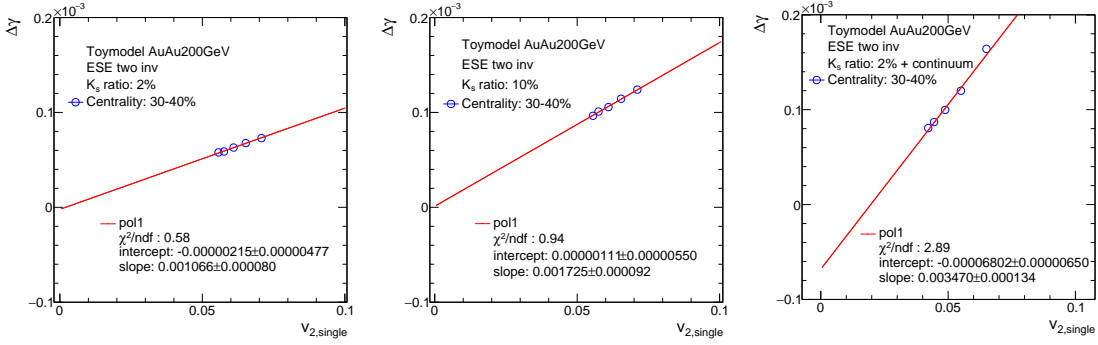


FIG. A.12. Toy model ESE results. Toy Model I with the accepted K_S fraction of the default 2% (left panel, 3×10^9 events) and of 10% (middle panel, 2×10^9 events), and Toy Model II with mass continuum (right panel, 10^8 events). The K_S , ρ^0 , and primordial pion inputs are from parameterizations to experimental data of 30–40% centrality Au+Au collisions at $\sqrt{s_{NN}} = 200$ GeV. The $\Delta\gamma$ is plotted as a function of v_2 in events binned in $\hat{q}_2^2\{2\}$ (Eqs. 5,6). POIs are from acceptance $0.3 < |\eta| < 1$, and the event selection variable $\hat{q}_2^2\{2\}$ is computed from particles in $|\eta| < 0.3$, both with $0.2 < p_T < 2$ GeV/c. The model's known impact parameter direction $\psi = 0$ is taken as the EP in calculating $\Delta\gamma$ (Eqs. 2,3) and $\langle v_2 \rangle$ (Eq. 10).

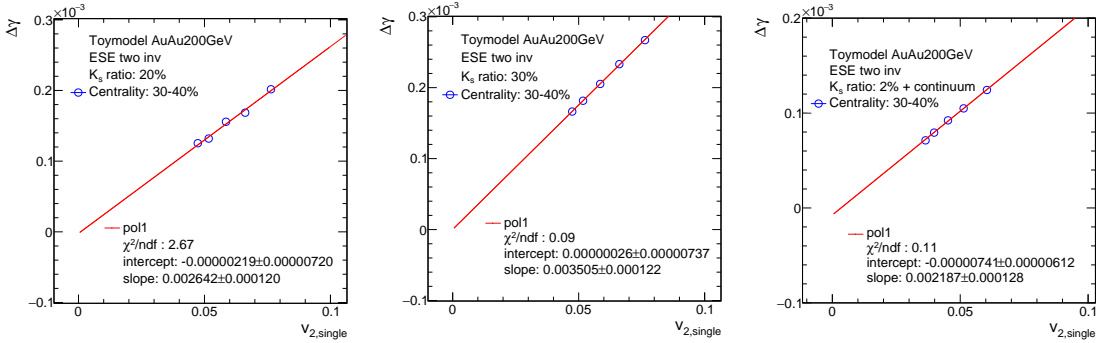


FIG. A.13. Toy model ESE results (forward/backward rapidity \hat{q}_2^2). Toy Model I with the accepted K_S fraction of 20% (left panel, 2×10^8 events) and of 30% (middle panel, 2.2×10^8 events), and Toy Model II with mass continuum (right panel, 10^8 events). The K_S , ρ^0 , and primordial pion inputs are from parameterizations to experimental data of 30–40% centrality Au+Au collisions at $\sqrt{s_{NN}} = 200$ GeV. The $\Delta\gamma$ is plotted as a function of v_2 in events binned in $\hat{q}_2^2\{2\}$ (Eqs. 5,6). POIs are from acceptance $0.3 < |\eta| < 1$, and the event selection variable $\hat{q}_2^2\{2\}$ is computed from particles in $3 < |\eta| < 4$, both with $0.2 < p_T < 2$ GeV/c. The model's known impact parameter direction $\psi = 0$ is taken as the EP in calculating $\Delta\gamma$ (Eqs. 2,3) and $\langle v_2 \rangle$ (Eq. 10).